1 # Calcium depletion challenges endoplasmic reticulum proteostasis by
2 destabilising BiP-substrate complexes
3

4 Steffen Preissler[1,2], Claudia Rato[1], Yahui Yan[1], Luke A. Perera[1], Aron Czako[1], David Ron[1,2]
5

6 [1]Cambridge Institute for Medical Research, University of Cambridge, Cambridge CB2 0XY,
7 United Kingdom
8 [2]Address correspondence to: Steffen Preissler, David Ron
9
10

Abstract

The metazoan endoplasmic reticulum (ER) serves both as a hub for maturation of secreted proteins and as an intracellular calcium storage compartment, facilitating calcium release-dependent cellular processes. ER calcium depletion robustly activates the unfolded protein response (UPR). However, it is unclear how fluctuations in ER calcium impact organellar proteostasis. Here we report that calcium selectively affects the dynamics of the abundant metazoan ER Hsp70 chaperone BiP, by enhancing its affinity for ADP. In the calcium replete ER, ADP rebinding to post-ATP hydrolysis BiP-substrate complexes competes with ATP binding during both spontaneous and co-chaperone-assisted nucleotide exchange, favouring substrate retention. Conversely, in the calcium depleted ER, relative acceleration of ADP-to-ATP exchange favours substrate release. These findings explain the rapid dissociation of certain substrates from BiP observed in the calcium-depleted ER and suggest a mechanism for tuning ER quality control and coupling UPR activity to signals that mobilise ER calcium in secretory cells.

Introduction

28 The endoplasmic reticulum (ER) of eukaryotic cells is a hub for synthesis and processing of

29 most secreted and membrane proteins. The maturation of these ER clients involves their *N*-

30 glycosylation, thiol oxidation, folding, and the assembly of multiprotein complexes. Oxidative

31 folding is error-prone and requires assistance by ER-resident molecular chaperones and

32 oxidoreductases. A signal transduction pathway, the unfolded protein response (UPR),

33 regulates ER protein folding capacity by adjusting the expression of chaperones and other

34 quality control factors to match the load of unfolded proteins (Walter and Ron, 2011). ER

35 stress, defined as a condition of excess unfolded ER client proteins over the capacity of the

36 folding machinery, activates UPR signalling to re-establish proteostasis.

37 The ER of animal cells is distinct in maintaining a high concentration of calcium (Ca^{2+})

38 compared to the surrounding cytoplasm (Alvarez and Montero, 2002; Bygrave and Benedetti,

39 1996; Meldolesi and Pozzan, 1998; Solovyova and Verkhratsky, 2002). Transient Ca^{2+} release

40 from the ER during signalling events controls numerous processes including gene expression

41 and exocytosis (Carreras-Sureda et al., 2018; Raffaello et al., 2016). It has long been known

42 that pharmacological manipulations (Macer and Koch, 1988; Welch et al., 1983; Wong et al.,

43 1993; Wu et al., 1981) and even physiological cues that deplete ER Ca^{2+} (Sans et al., 2002)

44 activate the UPR transducers, but the role of proteostatic challenge in UPR activation under

45 these conditions remains unclear.

46 The folded state of some ER clients, like the low-density lipoprotein receptor (Fass et al., 1997),

47 is stabilised by binding Ca^{2+} as a ligand. However, the contribution to UPR activity by the

48 proteostatic challenge arising from the mass of proteins whose maturation is directly

49 compromised by low ER Ca^{2+} (Cooper et al., 1997; Guest et al., 1997; Lodish and Kong, 1990;

50 Lodish et al., 1992; Pena et al., 2010) is unknown.

51 Components of the ER protein folding machinery have low-affinity Ca^{2+} binding sites, whose

52 occupancy is likely to decrease upon ER Ca^{2+} depletion within the physiological range.

53 Examples are the lectin-like chaperones calnexin (CNX) and calreticulin (CRT) (Baksh and

54 Michalak, 1991; Wada et al., 1991), Grp94 (Macer and Koch, 1988; Van et al., 1989), and

55 protein disulphide isomerase (PDI) (Lebeche et al., 1994; Lucero et al., 1994; Macer and Koch,

56 1988). These low-affinity binding sites are often found on N- or C-terminal extensions of the

57 aforementioned proteins, a feature consistent with the observation that their core functions as

58 chaperones or oxidoreductases are not known to be measurably affected at Ca^{2+} levels expected

59   in the depleted ER. In the ER, the functionality of these components might be altered, for
60   example through the effects of changing [Ca^{2+}] on their mobility or spatial distribution (Avezov
61   et al., 2015; Corbett et al., 1999), but presently the significance of this feature remains
62   unknown. Upon Ca^{2+} release from the ER, changes to cytoplasmic [Ca^{2+}] may have important
63   indirect effects on the ER environment (Groenendyk et al., 2014), but as these are mediated
64   via changes in gene expression, their inherent latency precludes an important contribution to
65   the rapid post-translational activation of UPR transducers observed in calcium depleted cells
66   (Bertolotti et al., 2000; Harding et al., 1999; Wong et al., 1993).

67   Against this background, we were intrigued by the behaviour of the abundant Hsp70-type ER
68   chaperone BiP upon depletion of ER Ca^{2+}. Release of ER Ca^{2+} has long been known to correlate
69   with disruption of certain BiP-substrate complexes (Suzuki et al., 1991). Such dissociation
70   occurs very rapidly, on the time-scale of minutes (Preissler et al., 2015), which is inconsistent
71   with a process driven by the slow build-up of competing unfolded newly-synthesised proteins.
72   ER Ca^{2+} depletion is also associated with the appearance of more BiP oligomers (Preissler et
73   al., 2015). As chaperoning of unfolded proteins by BiP competes with BiP oligomerisation, the
74   presence of more BiP oligomers is not easy to reconcile with a model whereby a proteostatic
75   challenge arising from the destabilisation of Ca^{2+}-binding secreted proteins, or compromised
76   functionality of parallel chaperone systems (e.g. CNX/CRX, PDI), is the major perturbation to
77   ER function imposed by low [Ca^{2+}].

78   These considerations have led us to revisit the effect of ER Ca^{2+} depletion on BiP function in
79   cells and in vitro. Here we report on a molecular basis of ER [Ca^{2+}]-dependent regulation of
80   BiP's functional dynamics under physiological conditions. Our observations provide a
81   plausible explanation for the rapid dissociation of BiP from substrates noted upon ER Ca^{2+}
82   depletion and suggest a chain of causality, whereby a primary effect of [Ca^{2+}] on BiP's
83   chaperone cycle gives rise to a secondary proteostatic challenge in the ER.

84

Results

Divergent effects of ER Ca²⁺ depletion and ER proteostatic challenge on trafficking of a model BiP substrate protein

To gauge the effect of ER Ca²⁺ depletion on trafficking of a model BiP substrate protein through the secretory pathway to the plasma membrane, we chose the T-cell antigen receptor α chain (TCRα). In absence of other TCR complex subunits the luminal part of this transmembrane protein interacts with BiP as a substrate and is retained in the ER (Suzuki et al., 1991). The reporter consisted of a cleavable, N-terminal ER targeting signal sequence fused to a FLAG-M1 sequence and the ectoplasmic/luminal domain of murine TCRα, followed by a transmembrane domain and a cytosolically-localised turquoise fluorescent protein (Tq) (Figure 1A). Since the transmembrane domain of TCRα contains a motif that leads to rapid ER-associated degradation of the orphan subunit (Bonifacino et al., 1990), it was replaced in this reporter by the transmembrane domain of the interleukin 2 receptor α subunit (Bonifacino et al., 1991). We anticipated that reporter transport would expose FLAG-M1 on the cell surface, making it accessible for immunostaining in non-permeabilised cells. Further stringency is imparted by the primary FLAG-M1 antibody that only recognises the epitope on the free N-terminus of TCRα following signal sequence removal. The turquoise fluorescence signal is thus a measure of reporter expression, while the FLAG-M1 signal is specific to the surface-exposed fraction.

Treatment of a CHO-K1 cell line stably expressing the TCRα reporter with thapsigargin (Tg), an agent that causes selective loss of ER Ca²⁺ by inhibiting the ER Ca²⁺ pump SERCA (Sagara and Inesi, 1991; Thastrup et al., 1990), led to a conspicuous increase of the FLAG-M1 signal, consistent with retention of the reporter in the ER under normal conditions and its Ca²⁺ depletion-induced migration to the cell surface (Figure 1B), as previously noted (Suzuki et al., 1991).

The TCRα ectoplasmic domain might be subject to multiple competing quality control processes in the ER as it contains several glycosylation sites that may also engage lectin chaperones. To focus the reporter on BiP-mediated regulation, all four glycosylation sites were removed (by single amino acid substitutions), generating a reporter (TCRα-N/Q) that was more tightly retained intracellularly under basal conditions and exposed on the cell surface upon ER Ca²⁺ release (Figure 1A and B).

116   Importantly, both wildtype TCRα and TCRα-N/Q co-immunoprecipitated with BiP and the

117   interaction was diminished in Tg-treated cells (Figure 1C). Binding of ATP to BiP lowers its

118   affinity for substrates and enhances their dissociation (Gaut and Hendershot, 1993; Munro and

119   Pelham, 1986), a feature common to the Hsp70 chaperone family. Addition of ATP to the cell

120   lysates strongly decreased co-precipitation of both reporters with BiP, consistent with their

121   binding to BiP as typical substrates (Figure 1C). Of note, more BiP was bound to TCRα-N/Q

122   compared to the wildtype version, suggesting that the fate of the mutant reporter more strongly

123   depends on its association with BiP (Figure 1C, compare lanes 2 and 5). These results agree

124   with a scenario whereby retention of the TCRα proteins in the ER is mediated by their

125   interaction with BiP and Ca^{2+} depletion leads to reporter dissociation from BiP, facilitating ER

126   exit and appearance on the cell surface (Suzuki et al., 1991).

127   This interpretation was further corroborated by the observation that Tg-induced progression of

128   the reporters to the plasma membrane was blocked by brefeldin A (Figure 1-figure supplement

129   1), which disrupts vesicular transport between ER and the Golgi apparatus (Lippincott-

130   Schwartz et al., 1989). Moreover, reporter exposure on the cell surface accrued gradually over

131   several hours (Figure 1-figure supplement 2), consistent with the kinetics of vesicular transport

132   between ER and the cell surface (Chen et al., 2013; Hirschberg et al., 1998; Suzuki et al., 1991).

133   Next, we examined whether reporter display on the plasma membrane could also arise from an

134   increased burden of misfolded ER proteins, or if it is a feature specifically related to low ER

135   Ca^{2+}. We used TCRα-N/Q for these experiments due to its improved ER retention

136   characteristics. Depletion of ER Ca^{2+} with the ionophore A23187 also led to accumulation of

137   the reporter on the cell surface (Figure 1D). In contrast, the reporter remained intracellular

138   upon treatment with tunicamycin (Tm) or 2-deoxyglucose (2DG) — compounds that cause

139   protein misfolding in the ER by interfering with N-glycosylation (Kozutsumi et al., 1988;

140   Kurtoglu et al., 2007). These observations suggest that release of the reporter's retention by

141   Ca^{2+} depletion can be uncoupled from a general proteostatic challenge.

142   To further address the relationship between proteostatic challenge, Ca^{2+} depletion, and TCRα-

143   N/Q trafficking, we temporally separated the perturbation to ER protein folding from Ca^{2+}

144   depletion. Treatment of cells with Tm before addition of Tg diminished ER Ca^{2+} depletion-

145   induced reporter exposure on the cell surface (Figure 1E, compare bars 2 and 4). Furthermore,

146   pharmacological inhibition of basal PERK activity, which increases substrate protein load in

147   the ER [by dysregulating the influx of newly-synthesised proteins (Harding et al., 2012)], had

148   a similar effect. The combined application of Tm and PERK inhibitor almost fully blocked

149   subsequent Tg-induced reporter trafficking (Figure 1E, bar 6). Thus, ER stress caused by

150   accumulation of unfolded proteins seems to disfavour Ca^{2+} release-mediated reporter export.

151   However, despite their divergent effects on reporter redistribution, both Ca^{2+} depleting agents

152   and glycosylation inhibitors robustly activated of UPR (Figure 1F and 1-figure supplement 3).

153   These findings hint at a qualitative difference between UPR induction caused by proteostatic

154   challenge and Ca^{2+} depletion.

Ca^{2+} decelerates BiP's ATPase cycle

156   The dissociation of BiP from model substrates emerges as an intriguing feature that

157   distinguishes ER Ca^{2+} depletion from manipulations that are known to primarily pose a

158   proteostatic challenge. BiP has been shown to bind Ca^{2+} (Lamb et al., 2006; Lievremont et al.,

159   1997; Macer and Koch, 1988), but a designated Ca^{2+} binding site has not been identified (see

160   below). We therefore set out to investigate the effect of Ca^{2+} on BiP function using cell-free

161   approaches.

162   Like typical Hsp70s, BiP consists of an N-terminal nucleotide binding domain (NBD) and C-

163   terminal substrate binding domain (SBD) connected by a hydrophobic linker peptide (Figure

164   2A). The binding of BiP to its substrates is subject to an ATP binding- and hydrolysis-

165   dependent allosteric chaperone cycle. In the ATP-bound state, the NBD and SBD are docked

166   against each other and the SBD adopts an open conformation, allowing fast exchange of

167   substrates. ATP hydrolysis to ADP causes domain undocking and closure of the SBD, leading

168   to tight substrate binding. Nucleotide exchange resets the cycle and triggers substrate release.

169   Under physiological conditions (i.e. in excess of ATP), ATP hydrolysis is considered the rate-

170   limiting step of the cycle due to BiP's low intrinsic ATPase activity. However, ER-resident J-

171   domain proteins (JDP) enhance BiP's ATP hydrolysis rate, whereas nucleotide exchange

172   factors (NEF) stimulate ADP release (Behnke et al., 2015).

173   ATP turnover is a global measure of BiP's activity and is reflected in rates of ADP production.

174   A kinetic assay detecting oxidation of nicotinamide adenine dinucleotide (NADH) that is

175   enzymatically coupled to ADP production, confirmed BiP's known low basal ATPase activity

176   and its stimulation by wildtype JDP cofactor, whereas a non-functional version, JDP^{QPD},

177   carrying a H-to-Q mutation in the conserved HPD motif of the J-domain (Wall et al., 1994),

178   did not stimulate BiP's ATPase activity (Figure 2B). Reaction velocity scaled with BiP

179   concentration, confirming that the assays were performed under non-saturating conditions

180   (Figure 2-figure supplement 1). Addition of $CaCl_2$ [to reactions containing magnesium (Mg^{2+})]

181   did not significantly alter BiP's basal ATPase rate but inhibited its JDP-stimulated activity by

182   ~30% (Figure 2B). The latter may be explained by competition between Ca^{2+} and Mg^{2+} for

183   nucleotides — a CaATP pool is more likely to expose its competitive effect on productive

184   MgATP binding to BiP at JDP-accelerated ATPase rates. This is consistent with the

185   requirement of Mg^{2+} for BiP's ATPase activity (Kassenbrock and Kelly, 1989).

186   These observations seemingly disagree with earlier reports of inhibition of BiP's basal ATPase

187   activity by Ca^{2+} (Kassenbrock and Kelly, 1989; Wei and Hendershot, 1995). Such differences

188   may relate to the fact that ADP was allowed to accumulate in the assays performed previously,

189   whereas here it was continuously depleted (and ATP regenerated) by the coupled NADH

190   oxidation. However, it is plausible that the presence of ADP might be physiologically relevant

191   and thus important to expose the effect of Ca^{2+} on BiP's function observed in vivo.

192   Corroborating this hypothesis, it has been shown that ADP and Ca^{2+} may modulate each other's

193   affinity for BiP (Lamb et al., 2006). Futhermore, recent reports suggest physiological

194   fluctuations in ER luminal nucleotide composition, with lower ATP concentrations in the ER

195   compared with mitochondria and the cytoplasm (Depaoli et al., 2018; Vishnu et al., 2014; Yong

196   et al., 2019), hinting at a variable and relatively low luminal ATP:ADP ratio.

197   We therefore turned to an assay that detects orthophosphate production and allows

198   measurement of ATPase activity in presence of ADP. The basal ATPase activity of BiP (at 3

199   mM $MgCl_2$ and 2 mM ATP) was only slightly affected when up to 1.6 mM $CaCl_2$ was added

200   (Figure 2C). However, in presence of 0.5 mM ADP ([ATP]/[ADP] = 4) titration of $CaCl_2$

201   showed a clear inhibitory effect, lowering the average ATPase rate of BiP by ~44% at the

202   highest [$CaCl_2$]. Ca^{2+}-dependent inhibition was slightly enhanced at 1 mM ADP ([ATP]/[ADP]

203   = 2), with a reduction by ~51%. This was observed in the context of generally lower ATPase

204   rates measured in presence of ADP, which directly competes with ATP for binding to BiP. The

205   dependence of Ca^{2+}-mediated inhibition on ADP suggested an important effect of Ca^{2+} on the

206   nucleotide exchange phase of BiP's ATPase cycle.

Ca^{2+} favours binding of ADP over ATP to BiP

207

208   Based on the above observations we investigated the effect of Ca^{2+} on ADP release — the first

209   step of nucleotide exchange (Figure 2A). Complexes between BiP and MABA-ADP [an ADP

210   analogue whose fluorescence intensity is enhanced when bound to Hsp70s (Theyssen et al.,

211   1996)] were allowed to form, and the decrease in fluorescence as MABA-ADP dissociated in

212   presence of an excess of non-fluorescent nucleotides was measured. In presence of 3 mM

213   MgCl$_2$, the basal rate of MABA-ADP release from BiP (k_{off} 0.0865 ± 0.0045 s^{-1}) was similar

214   to values reported earlier (Figure 3A) (Mayer et al., 2003; Preissler et al., 2017). When added

215   during the dissociation phase, CaCl$_2$ (up to 1 mM) had little effect on MABA-ADP release.

216   However, when included alongside the MABA-ADP (and 3 mM MgCl$_2$) during the loading

217   phase, Ca^{2+} strongly inhibited release in the subsequent dissociation step (decreasing the k_{off}

218   ~5.1-fold to 0.0171 ± 0.0004 s^{-1}) (Fig 3A, compare traces 2 and 3).

219   Importantly, titrating CaCl$_2$ during MABA-ADP binding to BiP (in presence of 3 mM MgCl$_2$)

220   yielded a half maximal inhibitory concentration (IC$_{50}$) of 82.3 ± 16.4 µM (Figure 3B). This

221   value fits well into the estimated range of physiological free Ca^{2+} fluctuations (from >100 µM

222   to low micromolar concentrations) in the ER and suggests that this effect could indeed be

223   relevant to BiP function in vivo.

224   The NEF, Grp170, enhanced nucleotide release and its net stimulatory effect was considerably

225   greater when BiP•MABA-ADP complexes were formed in presence of CaCl$_2$ [~3.1-fold

226   (Mg^{2+} alone) vs. ~11.1-fold (Ca^{2+} and Mg^{2+})] (Figure 3A, compare traces 1 and 4; 3 and 5).

227   As expected, in samples containing only CaCl$_2$, baseline MABA-ADP release was even slower

228   (k_{off} 0.0098 ± 0.0007 s^{-1}) and the Grp170-mediated stimulation was enhanced further (~14.7-

229   fold) (Figure 3-figure supplement 1). The role of NEFs in BiP's chaperone cycle may therefore

230   be particularly important at the high Ca^{2+} levels of the resting ER.

231   To explore the affinities of BiP for nucleotides in presence of Mg^{2+} or Ca^{2+}, the association and

232   dissociation rates of MABA-labelled ADP and ATP were compared. Complexes were allowed

233   to form in presence of either cation. To avoid the confounding effects of ATP hydrolysis, an

234   ATPase-deficient BiP^{T229A} mutant was also used (Gaut and Hendershot, 1993). In Ca^{2+}-

235   containing samples the dissociation of MABA-ADP from wildtype BiP was again slower,

236   while the association rate was slightly enhanced, resulting in a ~7.5-fold lower dissociation

237   constant (K_D) for ADP binding to BiP in presence of Ca^{2+} compared to Mg^{2+} (Figure 3C, grey

238   bars). MABA-ADP bound to BiP^{T229A} with a similar K_D (although the rates were somewhat

239   higher), indicating that the T229A mutation does not have a major global impact on BiP's

240   nucleotide binding properties (Figure 3C, red bars). MABA-ATP dissociation from BiP^{T229A}

241   was unaffected by Ca^{2+}, but its association was conspicuously slower, leading to a ~3.2-fold

242   higher K_D for MABA-ATP binding to BiP in presence of Ca^{2+} (Figure 3C, blue bars). Thus,

243   Ca^{2+} has opposite effects on the binding of ADP and ATP to BiP: it enhances BiP's affinity for

244   ADP while decreasing the affinity for ATP.

245   It has been proposed, based on differential scanning and isothermal titration calorimetry data,

246   that Ca^{2+} and Mg^{2+} bind cooperatively with ADP or ATP to BiP (each in a 1:1 stoichiometry)

247   and that both cations occupy the same or overlapping sites in the NBD (Lamb et al., 2006).

248   Our findings agree with these conclusions and suggest that Ca^{2+} and Mg^{2+} compete for

249   cooperative binding with either nucleotide to BiP. Moreover, the nucleotide release

250   experiments presented here indicate that Ca^{2+}'s effect is played out during BiP•nucleotide

251   complex formation rather than by cation swap on existing BiP•nucleotide complexes. In

252   presence of large excess of Mg^{2+} and ATP, productive binding of MgATP to Hsp70s is fast

253   and does not limit the rate of re-entering another round of ATP hydrolysis. However, our

254   observations suggest that the presence of Ca^{2+} favours futile ADP-to-ADP exchange,

255   attenuating the cycle. This non-productive nucleotide exchange might, to some extent, be

256   further promoted by a CaATP pool that competes with MgATP for BiP binding. Thus, at

257   expected physiological ATP:ADP ratios in the ER, Ca^{2+} has a substantial impact on the kinetics

258   of BiP's ATPase cycle and stands to influence its chaperone activity.

Ca^{2+} stabilises interactions between BiP and substrates

260   The rate of ADP-to-ATP exchange limits the kinetics with which BiP dissociates from its

261   substrates (Figure 2A). This implies that non-productive ADP exchange cycles, favoured by

262   Ca^{2+}, might also affect BiP-substrate interactions. We used biolayer interferometry (BLI) to

263   monitor the JDP-mediated binding of BiP to immobilised substrate on the surface of a sensor.

264   This approach tracks transient BiP-substrate interactions in real-time (Preissler et al., 2017). A

265   biotinylated J-domain (from ERdJ6) was co-immobilised together with a substrate peptide

266   [P15, (Misselwitz et al., 1998)] on streptavidin-coated BLI sensors (Figure 4A). These were

267   then transferred to solutions containing BiP to detect its association, followed by introduction

268   into solutions without BiP to detect its dissociation. The large number and heterogeneity of

269   potential BiP binding sites on protein-coated sensors provides a good means to study the

270   substrate binding characteristics of BiP (Preissler et al., 2017). Fast recruitment of BiP was

271   observed in presence of ATP and Mg^{2+} (Figure 4A, traces 1-5). This interaction was dependent

272   on J-domain-stimulated ATP hydrolysis, as the BiP binding signal was weak in presence of a

273   non-functional J-domain (J^{QPD}) [Figure 4A, trace 6 and (Preissler et al., 2017)]. Though slightly

274   slower, BiP recruitment was also efficient in presence of Ca^{2+} ($[MgCl_2]/[CaCl_2] = 3$),

275   suggesting that Ca^{2+} competes only weakly with Mg^{2+} under these conditions (Figure 4A, trace

276   2); consistent with slower cooperative binding of CaATP to BiP, compared to MgATP, and the

277   absence of an allosteric effect of Ca^{2+} on ATP binding- and hydrolysis-dependent substrate

278   interactions.

279   BiP molecules bound to the sensor via high-affinity substrate interactions are, by definition, in

280   a post-hydrolysis state — either ADP-bound or nucleotide-free (apo). Thus, BiP dissociation

281   is subject to nucleotide exchange events and is accelerated by ATP binding. Accordingly, in

282   Mg^{2+}-containing solutions, BiP dissociation was slow in presence of ADP and fast in presence

283   of ATP. When present in the dissociation phase, the combination of Mg^{2+} and Ca^{2+}

284   ([$MgCl_2$]/[$CaCl_2$] = 3) did not affect the rate of ATP-induced BiP dissociation from sensors

285   (Figure 4A, trace 3). Dissociation of BiP was also fast in a solution containing ATP and Ca^{2+}

286   as the only divalent cation, indicating that CaATP is able to allosterically trigger BiP

287   dissociation from its substrates (Figure 4A, trace 5). Given that Ca^{2+} slows down the binding

288   of ATP to BiP (Figure 3C), it seemed surprising that the average dissociation rate was slightly

289   higher compared to MgATP-induced BiP dissociation. This finding might be explained by poor

290   hydrolysis of CaATP, countering the contribution of ATP-hydrolysis-dependent re-

291   establishment of a stable BiP-substrate complex to the BLI signal arising in presence of the

292   hydrolysable MgATP.

293   In presence of Mg^{2+} and both ATP and ADP ([ATP]/[ADP] = 2), the dissociation of BiP from

294   J-domain- and P15-coated BLI sensors was slower compared to a solution containing only

295   Mg^{2+} and ATP, consistent with direct competition of ADP with ATP for binding to BiP (Figure

296   4B, trace 3). Addition of Ca^{2+} ([$MgCl_2$]/[$CaCl_2$] = 3) to a solution containing both nucleotides

297   further inhibited dissociation of BiP (Figure 4B, trace 4). This result agrees with the notion that

298   Ca^{2+} kinetically extends futile nucleotide exchange cycles by enhancing the affinity of ADP

299   (but not ATP) for BiP.

300   To dissect this further, BiP•substrate complexes were assembled on J-domain- and P15-coated

301   BLI sensors (in presence of MgATP, as above) followed by two sequential dissociation steps.

302   The BiP-loaded sensors were first introduced into solutions containing ADP and either Mg^{2+}

303   or Ca^{2+} to promote formation of BiP•MgADP•substrate or BiP•CaADP•substrate complexes,

304   which represent the expected intermediates of futile nucleotide exchange. The sensors were

305   then transferred to solutions containing Mg^{2+} and ATP. BiP bound to a sensor that had been

306   exposed to Mg^{2+} and ADP dissociated twice as fast in the second step than BiP on a sensor that

307   had been exposed to Ca^{2+} and ADP (Figure 4B, compare traces 5 and 6). This observation

308   indicates that the slow release of CaADP kinetically limits ADP-to-ATP exchange and

309   consequently ATP-enhanced dissociation of BiP from substrates.

310   These observations suggest that changes in [Ca^{2+}] (within the physiological range) regulate

311   BiP's chaperone activity by modulating the kinetics of productive nucleotide exchange, and

312   thus the rates of substrate release and entry into the next ATPase cycle. These findings propose

313   a mechanism for the decline in BiP-substrate interactions observed upon ER Ca^{2+} depletion.

314   All other things being equal, at high [Ca^{2+}]$_{ER}$ (resting state) substrate dissociation is slower.

315   Release of Ca^{2+} from the ER accelerates ATP binding and substrate dissociation, whereas the

316   rate at which ATP hydrolysis-dependent substrate interactions are formed remains largely

317   unaffected. The acceleration of productive nucleotide exchange and substrate dissociation,

318   relative to substrate binding, partitions BiP from its substrates.

Selective responsiveness of ER-localised Hsp70s to Ca^{2+}

320   Ca^{2+} excursions within the range shown here to affect BiP activity are unique to the ER.

321   Therefore, we deemed it of interest to determine if regulation by Ca^{2+} is a feature selective to

322   ER-localised Hsp70 (i.e. BiP) or common to all Hsp70s, regardless of the Ca^{2+} environment in

323   which they operate. To this end, we produced and purified bacterial DnaK, the *Drosophila*

324   *melanogaster* homologue of BiP, as well as human cytosolic Hsp70 (HSPA1A) and Hsc70

325   (HSPA8).

326   As before, MABA-ADP complexes with the different Hsp70s were formed in presence of Mg^{2+}

327   and nucleotide release upon exposure to excess of ATP was measured. MABA-ADP release

328   rates varied between the different Hsp70s (Figure 5A, dark traces). Similar to mammalian BiP,

329   Ca^{2+} strongly inhibited MABA-ADP release from *Drosophila* BiP ($\sim$5.6-fold) but had a more

330   modest inhibitory effect on MABA-ADP release from DnaK ($\sim$1.4-fold), cytosolic Hsp70

331   ($\sim$1.6-fold), and Hsc70 ($\sim$2.0-fold) (Figure 5A). Thus, under these conditions, Ca^{2+} had the

332   strongest inhibitory effect on MABA-ADP release from BiP paralogues.

333   We also analysed JDP-mediated substrate interactions of the different Hsp70 proteins using the

334   BLI assay. Dissociation was performed in presence of Mg^{2+}, ATP, and ADP ([ATP]/[ADP] =

335   2). Further addition of Ca^{2+} had the strongest inhibitory effect on the dissociation of BiP ($\sim$1.8-

336   fold decreased dissociation rate) and *Drosophila* BiP ($\sim$2.1-fold decrease), whereas

337   dissociation of the other chaperones was affected to a lesser degree (Hsp70 $\sim$1.2-fold, Hsc70

338    $\sim$1.2-fold, DnaK $\sim$1.1-fold) (Figure 5B and C).

339   These observations suggest that sensitivity of nucleotide exchange and substrate interactions

340   to Ca^{2+} is a feature specific to BiP paralogues, perhaps having evolved as an adaptation to the

341   ER environment.

CaADP binding selectively affects BiP's structural stability

343   To establish if the selective effect of Ca^{2+} on ADP binding to BiP is reflected in the structure

344   of the complex, we purified the NBDs of mammalian BiP, Hsp70, and Hsc70 and co-

345   crystallised them with Ca^{2+} and ADP. High-resolution X-ray crystal structures were obtained

346   for all three NBDs (Table S1). In each case, additional density in the nucleotide binding cleft

347   indicated occupancy by ADP (Figure 6-figure supplement 1A) and the overall conformations

348   of the three NBDs were very similar (Figure 6A). Overlay of the BiP(NBD) structure with the

349   Hsp70(NBD) and Hsc70(NBD) structures revealed root-mean-squared deviations (RMSD) of

350   0.769 Å and 0.734 Å over the C_α alignment, respectively. Moreover, in each structure, Ca^{2+}

351   was identified in the nucleotide binding cleft, where it formed contacts to both phosphate

352   groups (α and β) of the nucleotide as well as indirect contacts to protein residues via several

353   water molecules (Figure 6A, inset). The position of the Ca^{2+} ion and the coordinated water

354   molecules were nearly identical in all three complexes and similar to a previously reported

355   lower-resolution structure of human BiP bound to CaADP (Wisniewska et al., 2010). In

356   contrast, the Mg^{2+} ion in an earlier NBD•Mg^{2+}•ADP structure coordinates only the β-phosphate

357   of ADP directly (Figure 6B, upper panel), which may contribute to the lower affinity of

358   MgADP compared to CaADP for NBD binding. The BiP(NBD)•Ca^{2+}•ADP complex also

359   resembled the structures of BiP(NBD)^{apo} and the NBD of BiP^{apo} containing both its NBD and

360   SBD (Figure 6-figure supplement 1B). The Ca^{2+} location is slightly shifted with respect to the

361   position of Mg^{2+} in structures that likely reflect the post-hydrolysis state, where the cation

362   coordinates orthophosphate (P_i) and the β-phosphate of ADP (Figure 6B, lower panel). The

363   latter is more similar to the configuration of Hsp70•MgATP complexes, where the Mg^{2+} is

364   located between the β- and γ-phosphate groups of ATP (Figure 6-figure supplement 1C). The

365   Ca^{2+} ion in a structure of human Hsp70(NBD) in complex with Ca^{2+}, ADP, and P_i occupies the

366   same position as Mg^{2+} in a post-hydrolysis state NBD structure (Figure 6-figure supplement

367   1D). Together, these findings reveal that Ca^{2+} participates in the coordination of ADP in the

368   NBD, which is consistent with cooperative binding of Ca^{2+} and nucleotide to BiP. The

369   structures also imply that binding of Ca^{2+} and Mg^{2+} is mutually exclusive. This is consistent

370   with evidence against replacement of Mg^{2+} by Ca^{2+} in the post-hydrolysis complex and with

371 evidence that Ca^{2+} binds together with ADP after release of the hydrolysis products (i.e. to the

372 apo NBD) in cycles of ADP rebinding. Our structures also revealed a second, surface-exposed

373 Ca^{2+} ion, which is unlikely to be involved in allosteric regulation (Figure 6-figure supplement

374 1E; see discussion).

375 The highly similar CaADP binding mode does not explain the stronger effect of Ca^{2+} on BiP

376 function compared to the other Hsp70s. However, the IC_{50} values for Ca^{2+}-dependent inhibition

377 of MABA-ADP release from the NBDs of Hsp70 (444.7 ± 80.5 µM) and Hsc70 (345.5 ± 71.1

378 µM) were much higher than from the NBD of BiP (57.1 ± 7.4 µM) (Figure 6C). The latter was

379 similar to the IC_{50} values of full-length BiP and the *Drosophila* BiP(NBD) (52.4 ± 8.1 µM)

380 (Figure 3B and Figure 6-figure supplement 2A). In contrast, the IC_{50} for inhibition of MABA-

381 ADP release from DnaK(NBD) by Ca^{2+} was so high (> 8 mM) that saturation was not reached

382 over the titration range (Figure 6-figure supplement 2A). Given that concentrations of Ca^{2+} in

383 the cytoplasm are in the nanomolar range, these results imply that the effect of Ca^{2+} on ADP

384 binding to cytoplasmic Hsp70s has limited physiological relevance. We also tested the NBD

385 of Kar2, the ER Hsp70 chaperone of yeast (*Saccharomyces cerevisiae*), which had a high IC_{50}

386 of 888.0 ± 233.6 µM (Figure 6-figure supplement 2A). Thus, regulation by Ca^{2+} seems specific

387 to metazoan BiP.

388 Despite their nearly identical CaADP-bound structures, BiP(NBD), Hsp70(NBD), and

389 Hsc70(NBD) share only 70% sequence identity. We speculated that structural variation that is

390 inapparent in the low-energy, crystallised state may nonetheless lead to functionally important

391 differences in thermodynamic stabilisation by Ca^{2+} and ADP. Differential scanning fluorimetry

392 (DSF) measurements revealed that binding of ADP to all NBDs substantially elevated their

393 melting temperatures (T_m), as observed previously for intact BiP (Lamb et al., 2006). The T_m

394 increased further in presence of Ca^{+2} (Figure 6D and 6-figure supplement 2B). Importantly, the

395 stabilising effect of Ca^{+2} was greatest for mammalian and *Drosophila* BiP(NBD), compared to

396 the cytosolic Hsp70(NBD)s. These findings suggest that CaADP binding to the NBD

397 selectively decreases the structural flexibility of the ER-localised Hsp70s and thereby

398 contributes to their observed greater affinity for ADP.

399 **Differential sensitivity of BiP oligomers and BiP•substrate complexes to Ca^{2+}**

400 The activity of BiP in the ER is subject to post-translational regulatory mechanisms, one of

401 which is the transient sequestration of substrate-free BiP into inactive oligomeric assemblies.

402 These homomeric BiP complexes are based on typical substrate interactions between the SBD

403   of one protomer and the interdomain linker of another protomer (Preissler et al., 2015). As a

404   consequence, all BiP molecules of an oligomer are in a post-hydrolysis (ADP-bound or apo),

405   domain-undocked state (Figure 7A). These features entail a chain-like configuration where

406   only the first BiP molecule ('A') can bind substrate, whereas the SBDs and linkers of all

407   internal protomers ('B') are occupied. Apart from the last molecule ('C'), which exposes a free

408   linker, all other protomers are conformationally locked and therefore considered functionally

409   inactive. This model also predicts that oligomer assembly and disassembly occurs mainly on

410   one end and involves the 'C' protomer because it provides a binding site for another BiP

411   molecule (in assembly) and is the only protomer able to undergo ATP-induced domain docking

412   (required for dissociation). We define this end of BiP oligomers as the 'plus' (+)-end in analogy

413   to the more dynamic end of cytoskeletal filaments (Figure 7A).

414   The strong propensity of BiP to form oligomers and their architecture is further supported by

415   structural data: despite lacking part of the flexible C-terminal SBD lid structure and a substrate

416   binding-weakening V461F mutation, we obtained crystals of BiP in multi-component mixtures

417   formed by substrate interactions between the SBD and the interdomain linker of adjacent

418   molecules in the crystal lattice (Figure 7B and Figure 7-figure supplement 1).

419   Due to their characteristics, BiP oligomers are in direct competition with binding of unfolded

420   substrates, which explains their disappearance during ER stress (Blond-Elguindi et al., 1993;

421   Preissler et al., 2015). This suggests a physiological role of oligomerisation in buffering folding

422   capacity by transient withdrawal of BiP from the pool of active chaperones during periods of

423   declining unfolded protein load. However, the surprising observation that BiP oligomers are

424   enhanced by ER Ca^{2+} depletion seems to contradict this function and remained unexplained so

425   far (Preissler et al., 2015). We revisited this phenomenon in light of the new insights gleaned

426   here.

427   BiP oligomers rapidly disassemble in vitro in presence of ATP. However, the hypothesised

428   process by which BiP oligomers form and disassemble, described above, predicts that specific

429   inactivation of the 'C' protomer at the (+)-end would render them refractory to the destabilising

430   effect of ATP. We therefore took advantage of the protease subtilisin A (SubA), that cleaves

431   BiP site-specifically at the linker sequence (Paton et al., 2006). Under conditions that favour

432   oligomers, a large fraction of BiP is resistant to SubA cleavage (Preissler et al., 2015), likely

433   because only the linker of the 'C' protomer is accessible to the protease, whereas the linkers of

434   all other protomers are protected by an SBD of another BiP protein (Figure 7A). Indeed, size-

435   exclusion chromatography (SEC) analysis after exposure of BiP to SubA revealed a shift of all

436 peaks to later elution times, consistent with removal of a single NBD from oligomeric

437 structures and complete cleavage of monomers (Figure 7C).

438 We next formed complexes between BiP and fluorescently-labelled substrate peptide by

439 extended incubation of BiP (at a concentration where it is largely oligomeric) with trace

440 amounts of the peptide. The samples were then analysed by SEC and substrate peptide

441 fluorescence was detected separately from bulk protein absorbance at 230 nm (A_{230}), which is

442 vastly dominated by BiP. The peptide co-eluted with BiP monomers and oligomers (Figure

443 7D, left panels). The stepwise increase in the ratio of A_{230} to fluorescence signal with oligomer

444 size is consistent with each oligomeric species exposing only a single binding site [at its (-)-

445 end]. As expected, addition of ATP to the sample shortly before injection onto the SEC column

446 converted BiP oligomers largely into monomers, releasing the bound substrate peptide. As

447 noted previously, treatment with SubA prior to SEC, shifted the oligomer peaks to later elution

448 times and abolished the monomer signal in both the A_{230} and fluorescence channel. However,

449 in contrast to the intact oligomers, the cleaved species were completely insensitive to ATP-

450 induced disassembly and peptide release (Figure 7D, right panels). We conclude that

451 proteolytic removal of the NBD from the terminal protomer stabilises BiP oligomers by

452 inactivating their only conformationally responsive molecule, the 'C' protomer on the (+)-end.

453 These data also provide evidence for a strictly directional oligomer disassembly mode that

454 proceeds from the (+)-end.

455 Their inertness suggested the possibility of separating SubA-cleaved BiP oligomers from other

456 cleavage products by size to enable their biochemical characterisation (Figure 7D). To this end,

457 we incubated purified BiP protein at high concentration with SubA followed by preparative

458 SEC to isolate the early-eluting oligomeric species. Subsequent analytical SEC revealed that

459 the isolated cleaved oligomers retained their expected elution profile (Figure 7-figure

460 supplement 2) and proved resistant to ATP-induced disassembly (stable over 3 hours at 26°C),

461 and thus deemed suitable for further biochemical characterisation (Figure 7-figure supplement

462 2).

463 MABA-ADP (bound in presence of Mg^{2+}) dissociated from stabilised (SubA-cleaved) BiP

464 oligomers and untreated BiP at similar rates (Figure 7E). Addition of Ca^{2+} ([$MgCl_2$]/[$CaCl_2$] =

465 3) had a similar inhibitory effect on MABA-ADP dissociation from both samples. In contrast,

466 under these conditions, Grp170 enhanced the rate of MABA-ADP release from stabilised

467 oligomers only ~2.9-fold, whereas release from untreated BiP was enhanced ~12.3-fold

468 (Figure 7E). The latter is consistent with the experiments shown above (Figure 3A). These

469   results indicate (i) that passive nucleotide exchange occurs with normal rates on BiP oligomers

470   but their conformationally trapped state renders them non-responsive to ATP binding, and (ii)

471   that oligomers are largely resistant to Grp170-stimulated nucleotide release. Together with the

472   finding that BiP oligomers disassemble from one end, these observations suggest a mechanism

473   whereby the relative inertness of the internal protomers kinetically favours BiP oligomers over

474   other BiP-substrate interactions in the Ca^{2+}-depleted ER.

Discussion

475   The roles of BiP as an abundant effector chaperone and feedback regulator of the UPR render

476   it an essential guardian of ER physiology. Both functions converge on conventional Hsp70

477   substrate-binding interactions and are subordinate to the kinetics of nucleotide turnover by

478   BiP's ATPase activity. The finding that BiP's ATPase cycle is modulated by Ca^{2+} fluctuations

479   within the physiological range suggests a defined mechanism that links ER Ca^{2+} changes to

480   protein homeostasis. In the Ca^{2+}-depleted ER, BiP-substrate interactions are destabilised

481   (Figure 8). The partitioning of substrates away from the only luminal Hsp70 favours trafficking

482   of those substrates that would otherwise have been retained by BiP, whilst promoting de-

483   repression of the UPR transducers, themselves BiP substrates. The perturbation to ER

484   proteostasis is compounded by the polarity of BiP oligomers, which specifies their relative

485   inertness to Ca^{2+} fluctuations, thus kinetically driving BiP to oligomerise and depleting the

486   pool of active monomers. Alongside the direct role played by Ca^{2+} in the folding of certain

487   secreted proteins, and the role of Ca^{2+} binding to low affinity sites in regulating the in vivo

488   activity of parallel ER chaperones, the aforementioned mechanism goes some way to explain

489   the well-established relationship between ER Ca^{2+} depletion and the activation of ER stress

490   signalling.

491

492   Comparison of cytosolic and ER Hsp70s suggests that regulation of BiP by Ca^{2+} co-evolved

493   with the functions of the mammalian ER in Ca^{2+} storage and signalling. This is reflected in the

494   relative insensitivity of cytosolic and bacterial Hsp70s to Ca^{2+} and in apparent tuning of

495   metazoan BiP to the range of physiological ER Ca^{2+} fluctuations. In this vein, the yeast ER

496   Hsp70 Kar2, is of special interest, as we found it to be much less sensitive to Ca^{2+} than its

497   metazoan counter parts. This correlates with the yeast vacuole, not the ER, serving as the major

498   intracellular Ca^{2+} store responsible for regulated Ca^{2+} release (Denis and Cyert, 2002;

499   Halachmi and Eilam, 1989; Strayle et al., 1999).

500   At high CaADP concentrations, the crystallised NBDs of all Hsp70's tested bind the ion-

501   nucleotide complex indistinguishably. Solution-based assays suggest that subtle differences in

502   protein stability, arising from the 30% sequence divergence between the NBD of metazoan BiP

503   and its cytosolic counterparts, may account for their different sensitivity to Ca^{2+}. Regardless of

504   its structural basis, it is intriguing to consider how this specialised feature of BiP (conserved

505   from mammals to flies) improves fitness.

506　From the pancreatic acinus to killer T cells, secretion of proteins (stored in granules) is

507　regulated by Ca^{2+} release from the ER. The destabilising effect of Ca^{2+} depletion on BiP-

508　substrate complexes may have arisen as a response to situations in which the demands for bulk

509　protein export from the ER (to replenish secreted protein stores) outweighs the benefits of

510　stringent quality control (that would otherwise be imposed by more prolonged BiP-substrate

511　interactions and ER retention). ER quality control responds continuously to the thermodynamic

512　instability of its substrates (Sekijima et al., 2005). The dissociation of BiP from a class of not

513　yet natively assembled but export-ready substrates during Ca^{2+} signalling events may thus

514　reflect a mechanism for tuning the stringency of quality control to physiological demands.

515　Activation of the UPR transducers, IRE1, PERK, and ATF6 is a prominent consequence of ER

516　Ca^{2+} depletion. Disagreements on the details notwithstanding, most models for UPR regulation

517　acknowledge the importance of BiP-substrate interactions (Karagoz et al., 2019). In one model,

518　BiP is thought to bind directly to the regulatory luminal domain of the transducers via typical

519　BiP-substrate interactions, to keep it in a repressed state (Amin-Wetzel et al., 2019; Amin-

520　Wetzel et al., 2017). Competing substrates displace BiP from the signal transducers resulting

521　in their activation. The findings presented here imply that declining ER Ca^{2+} favours

522　dissociation of BiP from UPR signal transducers, which is consistent with previous pulldown

523　experiments showing release of BiP from PERK and ATF6 upon ER Ca^{2+} depletion (Bertolotti

524　et al., 2000; Shen et al., 2002). Importantly, BiP dissociation under these conditions is complete

525　on a timescale of minutes and does not require an ongoing supply of nascent unfolded proteins,

526　placing it upstream of any proteostatic challenge arising directly from Ca^{2+} depletion.

527　Similarly, dissociation of BiP from substrates may fuel the supply of activating ligands of the

528　UPR transducers (Karagoz et al., 2019). Physiological fluctuations of Ca^{2+} levels are often

529　oscillatory (Berridge et al., 2000; Dupont et al., 2011; Raffaello et al., 2016; Thomas et al.,

530　1996). The Ca^{2+}-entrained pulses of UPR signalling arising from the specialised sensitivity of

531　BiP to Ca^{2+} may have evolved to tune gene expression programs that build secretory capacity

532　to the secretory activity of cells. Given the reversibility of the Ca^{2+} effect on BiP and the

533　transient nature of physiological Ca^{2+} fluctuations, such conditioning of the ER is likely

534　attained without a significant cost of protein aggregation and proteotoxicity.

535　Our findings indicate that Ca^{2+} acts mainly on the nucleotide exchange phase of BiP's

536　chaperone cycle. After post-hydrolysis ADP release, ATP and ADP compete for binding to

537　BiP. Depending on the outcome of this competition BiP either enters a futile nucleotide

538　exchange cycle through ADP re-binding, or acquires ATP, which triggers substrate release.

539   Ca^{2+} enhances the affinity of ADP for BiP and thereby promotes the ADP-bound state during

540   nucleotide exchange. The efficiency of ADP-to-ATP exchange and rates of substrate release

541   are thus inversely related to $[Ca^{2+}]$. As BiP requires MgATP to re-enter its chaperone cycle

542   (Kassenbrock and Kelly, 1989), the rate at which ATP hydrolysis-dependent interactions with

543   substrates are formed remain largely unaffected by Ca^{2+}. This rationalises the observed

544   consequences of lowering free Ca^{2+} levels in the ER on the interactions of BiP with its

545   substrates: a decrease in $[Ca^{2+}]$ enhances the effective rate of ATP-induced substrate release

546   from BiP relative to the rate of substrate binding, leading to a net decline of BiP•substrate

547   complexes.

548   Our structural data show that Ca^{2+} binds in the nucleotide binding cleft of the NBD and

549   participates in coordinating the phosphate groups of ADP. This sufficiently explains the

550   observed cooperative binding mode of Ca^{2+} and nucleotide to BiP. Although none of our

551   functional experiments indicated that Ca^{2+} exerts an allosteric effect on BiP through a

552   mechanism other than by replacing Mg^{2+} during nucleotide binding, an additional Ca^{2+} ion was

553   present on the surface in all of our Hsp70 NBD structures. Ca^{2+} binding to this second site is

554   likely an experimental artefact favoured by the high $[Ca^{2+}]$ in the crystallisation solution and

555   crystal packing. Its relevance to any allosteric regulation of BiP is rendered improbable by the

556   high degree of solvent exposure of the bound Ca^{2+}.

557   Chaperones, in particular BiP, are the most abundant ATPases in the ER (Bakunts et al., 2017;

558   Dierks et al., 1996). Increasing protein folding load could thus boost ATP consumption by

559   chaperones and temporarily lower the luminal ATP:ADP ratio. Coupling regulation of BiP by

560   Ca^{2+} to the ATP:ADP ratio may therefore save energy at basally high luminal $[Ca^{2+}]$ by

561   amplifying the effect of ADP as a competitor for ATP and thus lowering BiP's ATPase activity.

562   Similar principles may apply to chaperone systems in other cellular compartments as well

563   (although there the impact of Ca^{2+} is most likely negligible).

564   In contrast, ER Ca^{2+} depletion might enhance BiP's ATPase activity. The cost of this to the ER

565   energy balance may be compensated (at least transiently) by an increase in ATP import into

566   the organelle (Vishnu et al., 2014; Yong et al., 2019). Furthermore, the effect on global

567   energetics is mitigated by PERK activation and the attendant decrease in energetically

568   expensive protein synthesis. In this sense, it is interesting to speculate that BiP's responsiveness

569   to Ca^{2+} is an animal cell feature that co-evolved with the acquisition of PERK.

570   Likewise, BiP oligomerisation may have evolved to alleviate the consequences of enhanced
571   ATP consumption at low Ca^{2+} levels by sequestering BiP in inactive complexes with relatively
572   slow turnover rates under these conditions. Mechanistically this can be explained by the finding
573   that BiP oligomer disassembly proceeds in a strictly directional manner and thus might be
574   relatively slow compared to the one-step dissociation of heterodimeric BiP•substrate
575   complexes. This difference is likely enhanced at low $[Ca^{2+}]$ when ADP-to-ATP exchange is
576   more efficient and the unidirectional, step-wise dissociation of BiP oligomers imposes an even
577   greater relative kinetic penalty, causing a redistribution of BiP from heterodimeric
578   BiP•substrate complexes to oligomers. Furthermore, conformationally trapped oligomeric BiP
579   is largely resistant to stimulated ADP release by Grp170, the most abundant NEF in the ER
580   (Behnke et al., 2015; Weitzmann et al., 2007). Grp170 belongs to the Hsp110 class of NEFs,
581   which bind Hsp70s via a large contact area (Polier et al., 2008). It is therefore possible that part
582   of the Grp170 binding site on BiP is sterically occluded in oligomers. The differential action
583   of Grp170 (and potentially other co-factors) on BiP•substrate complexes and oligomers likely
584   contributes to the altered BiP dynamics at varying Ca^{2+} levels.

585   Changes in BiP's substrate interaction kinetics are observed within minutes of ER Ca^{2+}
586   depletion (Preissler et al., 2015). The dissociation of substrates from BiP under conditions of
587   low $[Ca^{2+}]$ may allow some of them to escape retention in the ER and enhance their secretion.
588   This is supported by the behaviour of the BiP-interacting TCRα reporters, which migrated to
589   the cell surface after release of ER Ca^{2+} [Figure 1 and (Suzuki et al., 1991)]. TCRα trafficking
590   to the cell surface is not observed under conditions that primarily perturb protein folding
591   homeostasis, suggesting that this effect of ER Ca^{2+} depletion is not a consequence of
592   downstream proteostatic challenge. However, the dominance of the mechanistic link proposed
593   here for TCRα's itinerary remains unproven, as we are unable to establish a system in which
594   BiP's essential role as a chaperone is uncoupled from its responsiveness to Ca^{2+}. Moreover,
595   destabilisation of BiP-substrate interactions is likely not the only mechanistic connection
596   between ER Ca^{2+} release, enhanced protein trafficking, and UPR induction. The downstream
597   perturbation to protein folding arising from substrate release and partitioning to oligomers may
598   contribute, especially under experimental conditions of protracted ER Ca^{2+} depletion following
599   lengthy application of Ca^{2+}-mobilising agents or irreversible uptake inhibitors. The action of
600   such parallel mechanism is evident in the escape of misfolded prion precursor protein from the
601   ER quality control upon proteostatic challenge with a reducing agent (Satpute-Krishnan et al.,

602   2014). It should be interesting to define in molecular terms the basis for other condition-

603   dependent modulation of ER quality control.

604

Acknowledgements

We thank the CIMR flow cytometry facility for technical support, the James Huntington group (CIMR) for access to BLI equipment, Matthias P. Mayer (University of Heidelberg) for Hsp70 and Hsc70 expression plasmids, and Claes Andréasson (Stockholm University) for Grp170 expression plasmids. We are grateful to the Diamond Light Source for beamtime (proposals mx21426 and mx27082) and the staff of beamlines I03, I04 and I24 for assistance with data collection. We also thank Luka Smalinskaite for help with ATPase experiments as well as Alisa F. Zyryanova and Lisa Neidhardt for comments on the manuscript.

Author contributions

S.P. Conceptualisation, project administration, methodology, investigation, formal analysis, visualisation, and writing — original draft preparation.

C.R. Methodology, investigation, formal analysis, and writing — review and editing.

Y.Y. Investigation, formal analysis, data curation, visualisation, and writing — review and editing.

L.P. Investigation, formal analysis, data curation, and writing — review and editing.

A.C. Investigation and writing — review and editing.

D.R. Conceptualisation, methodology, funding acquisition, and writing — original draft preparation.

Competing interests

The authors declare no competing or financial interests.

Methods

DNA plasmids

The plasmids used in this study have been described previously or were generated by standard molecular cloning techniques and are listed in Table S2.

Mammalian cell lines

CHO-K1 cells (ATCC CCL-61) were phenotypically validated as proline auxotrophs and their Chinese hamster (*Cricetulus griseus*) origin was confirmed by genomic sequencing. The cells were grown on cell culture dishes or multi-well plates (Corning) at 37°C and 5% CO_2 in Nutrient mixture F-12 Ham (Sigma-Aldrich) supplemented with 10% (v/v) serum (FetalClone II; HyClone), 1× penicillin–streptomycin (Sigma-Aldrich), and 2 mM L-glutamine (Sigma-Aldrich). Cell lines were randomly tested for mycoplasma contamination using the MycoAlert Mycoplasma Detection Kit (Lonza). All experiments were performed at cell densities of 60–90% confluence. Where indicated, cells were treated with 0.5 µM Thapsigargin (Tg; Calbiochem), 2.5 µg/ml Tunicamycin (Tm; Melford), 10 µM A23187 (Sigma, C7522), 3 mM 2-deoxy-D-glucose (2DG; ACROS Organics), 2 µM PERK inhibitor (PERKi; gift from GSK, GSK2606414) and 10 µg/ml brefeldin A (BFA; LC Laboratories, B-8500). All compounds were diluted freshly in pre-warmed medium and applied to the cells by medium exchange.

The UPR reporter cell line CHO-K1 *CHOP::GFP XBP1::Turquoise* (clone S21) has been described previously (Sekine et al., 2016). Cell lines stably expressing TCRα and TCRα-N/Q were generated by targeting CHO-K1 cells with puromycin-resistant retrovirus. For that, HEK293T cells (ATCC CRL-3216) were cultured in Dulbecco's modified Eagle's medium (Sigma) supplemented as described above. The cells were split onto 6 cm-dishes 24 h prior to co-transfection of pBABE Puro plasmids encoding TCRα or TCRα-N/Q (plasmids UK2469 and UK2520, respectively; Table S2) with VSV-G retroviral packaging vectors, using TransIT-293 Transfection Reagent (Mirus) according to the manufacturer's instructions. Sixteen hours after transfection, medium was changed to medium supplemented with 1% BSA (Sigma). Retroviral infections were performed following a 24 h incubation period by diluting 0.45 µm filter-sterilised cell culture supernatants at a 1:1 ratio with CHO-K1 cell medium supplemented with 10 µg/ml polybrene (8 ml final volume) and adding this preparation to target CHO-K1 cells (1 x 10^6 cells seeded onto 10 cm-dishes 24 h prior to infection). After 8 h the viral supernatants were replaced with fresh medium. The cells were split 48 h later into medium supplemented with 6 µg/ml puromycin (Calbiochem). After further 24 h the medium was changed to medium supplemented with 8 µg/ml puromycin. The medium was changed every third day until puromycin-resistant colonies were visible. Individual clones were isolated and tested for reporter expression. CHO-K1 TCRα (clone 24) and CHO-K1 TCRα-N/Q (clone 12) were used for all experiments shown.

Flow cytometry

To analyse expression of TCRα and TCRα-N/Q reporters on the cell surface, stable CHO-K1 clones (see above) or parental cells were grown on 6-well plates to 80-90% confluence and treated as indicated. The cells were then washed with 1 ml PBS and incubated in 0.5 ml PBS + 2 mM EDTA for 5 min at 37°C. Afterwards, the cells were transferred to a 1.2 ml tube (STARLAB, I1412-7400) and pelleted for 3 min in a swing-out rotor at 1000 rpm in a tabletop centrifuge (Allegra X-30R, Beckman Coulter). The supernatant was aspirated and cells were

680   suspended in the remaining liquid to $1 \times 10^5 - 1 \times 10^7$ cells/100 µl. The cells were washed with
681   1 ml ice-cold TBS solution [TBS + 3% bovine serum albumin (BSA) + 2 mM $CaCl_2$ + 0.1%
682   NaN_3] and pelleted as above. The supernatant was removed entirely and cells were suspended
683   in 100 µl of the same TBS solution containing mouse monoclonal ANTI-FLAG M1 antibodies
684   (Sigma, F3040) at a 1:500 dilution. The cells were incubated 30 min on ice while gently mixing
685   every 10 min. After the incubation time, cells were washed twice in 1 ml TBS solution and
686   suspended in TBS solution containing Alexa Fluor 488 Goat anti-mouse IgG (Jackson
687   ImmunoResearch, 115-545-146; 0.75 mg/ml stock in 50% glycerol) at a 1:750 dilution for 30
688   min on ice in the dark as above. The cells were pelleted, washed with TBS solution and
689   suspended in 400 µl TBS solution for flow cytometry analysis. For analysis of UPR reporter
690   induction, CHO-K1 S21 cells were treated as indicated, washed with PBS and collected in PBS
691   containing 4 mM ethylenediaminetetraacetic acid (EDTA).

692

693   Single-cell fluorescence signals (20,000/sample) were analysed by dual-channel flow
694   cytometry with an LSRFortessa cell analyser (BD Biosciences). GFP fluorescence and Alexa
695   Fluor 488 fluorescence was detected with excitation laser 488 nm and a 530/30 emission filter
696   and Turquoise fluorescence was detected with excitation laser 405 nm and a 450/50 emission
697   filter. Data were processed using FlowJo and median reporter analysis was performed using
698   Prism 6.0e (GraphPad).

699

700   **Immonoprecipitation (IP) and immunoblotting**

701

702   Mammalian cells were grown on 10 cm dishes and treated as indicated. The dishes were then
703   placed on ice and washed with ice-cold PBS, and cells were detached in PBS containing 1 mM
704   EDTA using a cell scraper. The cells were sedimented for 5 min at $370 \times g$ at 4°C and lysed in
705   HG lysis buffer (20 mM HEPES-KOH pH 7.4, 150 mM NaCl, 2 mM $MgCl_2$, 10 mM D-
706   glucose, 10% glycerol, 1% Triton X-100) containing protease inhibitors [2 mM
707   phenylmethylsulphonyl fluoride (PMSF), 4 µg/ml pepstatin, 4 µg/ml leupeptin, 8 µg/ml
708   aprotinin] with 100 U/ml hexokinase (from *Saccharomyces cerevisiae* type F-300; Sigma) for
709   10 min on ice. To release BiP from substrates, hexokinase was replaced by 1 mM ATP during
710   lysis. The lysates were cleared for 10 min at $21,000 \times g$ at 4°C and Bio-Rad protein assay
711   reagent (Bio-Rad) was used to determine the protein concentrations of lysates. Equal volumes
712   of normalised lysates were incubated for 2 h at 4°C with 20 µl UltraLink Hydrazine Resin
713   (Pierce, 53149) on which hamster BiP-specific chicken IgY antibodies had been covalently
714   immobilised (Preissler et al., 2015). The beads were recovered by centrifugation for 1 min at
715      $1,000 \times g$ and washed three times (for 5 min) with HG lysis buffer. The proteins were eluted
716   in $2 \times$ SDS sample buffer and denatured for 10 min at 70°C. Equal volumes of the samples
717   were applied to SDS-PAGE and proteins were transferred onto PVDF membranes. The
718   membranes were blocked with 5% (w/v) dried skimmed milk in TBS and incubated with
719   primary antibodies followed by IRDye fluorescently labelled secondary antibodies (LiCor).
720   The membranes were scanned with an Odyssey near-infrared imager (LiCor). Primary
721   antibodies against hamster BiP [chicken anti-BiP IgY; (Avezov et al., 2013)] and ANTI-FLAG
722   M1 (see above) were used. The relevant signals were quantified with ImageJ (NIH) and
723   analysed with Prism 8.4 (GraphPad).

724

725   **Protein purification**

726

727   <u>BiP and stabilised oligomers</u>

728

729 Wildtype (UK173) and T229A mutant (UK838) Chinese hamster BiP proteins with an N-
730 terminal His6-tag were expressed in M15 *E. coli* cells (Qiagen). The bacterial cultures were
731 grown in LB medium with 100 μg/ml ampicillin and 50 μg/ml kanamycin at 37°C to an $OD_{600\ nm}$
732 of 0.8 and expression was induced with 1 mM isopropylthio β-D-1-galactopyranoside
733 (IPTG). The cells were further grown for 6 h at 37°C, collected and lysed with a high-pressure
734 homogeniser (EmulsiFlex-C3; Avestin) in buffer A (50 mM Tris–HCl pH 8, 500 mM NaCl, 1
735 mM $MgCl_2$, 10% glycerol, 20 mM imidazole) containing protease inhibitors (1 mM PMSF, 2
736 μg/ml pepstatin, 8 μg/ml aprotinin, 2 μM leupeptin) and 0.1 mg/ml DNaseI. The lysates were
737 cleared for 30 min at 45,000 × g at 4°C and incubated with 1 ml of Ni-NTA agarose beads
738 (Qiagen) per 1 l of expression culture for 2 h rotating at 4°C. Afterwards, the beads was
739 transferred to a gravity-flow Econo column (49 ml volume; Bio-Rad) and washed with 2
740 column volumes (CV) buffer B (50 mM Tris–HCl pH 8.0, 500 mM NaCl, 10% glycerol, 30
741 mM imidazole), 2 CV buffer C (50 mM Tris–HCl pH 8.0, 300 mM NaCl, 10 mM imidazole, 5
742 mM β-mercaptoethanol) and buffer C sequentially supplemented with (i) 1 M NaCl, (ii) 10
743 mM $MgCl_2$ + 3 mM ATP, (iii) 0.5 M Tris–HCl pH 7.4 or (iv) 35 mM imidazole (2 CV each).
744 The BiP proteins were then eluted with buffer D (50 mM Tris–HCl pH 8.0, 300 mM NaCl, 5
745 mM β-mercaptoethanol, 250 mM imidazole), dialysed against HKM (50 mM HEPES-KOH
746 pH 7.4, 150 mM KCl, 10 mM $MgCl_2$) and concentrated with 30-kDa MWCO centrifugal filters
747 (Amicon Ultra, Merck Millipore). The proteins were flash-frozen in aliquots and stored at
748 −80°C. To obtain nucleotide-free preparations, the purified proteins were additionally dialysed
749 24 h at 4°C against 50 mM HEPES-KOH pH 7.4, 150 mM KCl, 4 mM EDTA and twice against
750 50 mM HEPES-KOH pH 7.4, 150 mM KCl before concentration and freezing.
751
752 Stabilised BiP oligomers were generated from purified BiP protein (UK173). The proteins were
753 concentrated in HKM buffer to ~16 mg/ml and SubA protease (produced in-house) (Paton et
754 al., 2006) was added at 50 ng/μl. After incubation for 40 minutes at 26°C to allow for complete
755 cleavage, the sample was cooled on ice for 5 min. The solution was then cleared through a 0.22
756 μm pore size centrifuge tube filter (Spin-X, Corning) and injected onto a Superdex 200 Increase
757 10/300 GL column (GE Healthcare) equilibrated in 50 mM HEPES-KOH pH 7.4, 150 mM
758 KCl. The early eluting peak fractions containing oligomeric BiP species were immediately
759 pooled, concentrated and frozen in aliquots.
760
761 <u>Grp170 and authentic Hsp70s</u>
762
763 Full-length human Grp170 (UK2225), BiP from *Drosophila melanogaster* (UK2354) as well
764 as human Hsp70 (UK2510) and Hsc70 (UK2511) were expressed as fusion proteins with an
765 N-terminal His6-Smt3 in *E. coli* BL21 T7 Express lysY/Iq cells (New England BioLabs,
766 C3013). The cells were grown in LB medium containing 50 μg/ml kanamycin at 37°C until
767 $OD_{600\ nm}$ 0.5. The cells were then transferred to 20°C and expression was induced after 20 min
768 with 0.5 mM IPTG. After incubation for 14 h, the cells were collected by centrifugation and
769 suspended in lysis buffer E (50 mM Tris-HCl pH 8, 500 mM NaCl, 20 mM imidazole, 10%
770 glycerol) containing protease inhibitors (1 mM PMSF, 2 μg/ml pepstatin, 8 μg/ml aprotinin, 2
771 μM leupeptin). Before lysis 1 mM $MgCl_2$, 0.1 mM tris(2-carboxyethyl)phosphine (TCEP), and
772 0.1 mg/ml DNaseI were added and lysis was performed with an EmulsiFlex-C3 high-pressure
773 homogeniser. The lysates were cleared for 30 min at 45,000 × g at 4°C and incubated with 0.6
774 ml of Ni-NTA agarose beads (Qiagen) per 1 l of expression culture (1 ml beads per 1 l
775 expression culture was used in case of *Drosophila* BiP, Hsp70 and Hsc70) for 1 h rotating at
776 4°C. Afterwards, the beads were transferred to a 49-ml gravity-flow column and washed with
777 2 CV lysis buffer E, 2 CV buffer F (25 mM Tris–HCl pH 8, 150 mM NaCl, 10 mM imidazole,

778 5 mM β-mercaptoethanol), and buffer F sequentially supplemented with (i) 1 M NaCl, (ii) 10
779 mM MgCl$_2$ + 3 mM ATP + 0.01 mg/ml RNaseA, or (iii) 0.5 M Tris–HCl pH 8 + 1 mM TCEP
780 (2 CV each), followed by 2 CV buffer F. Proteins were eluted by on-column cleavage with 1.5
781 µg/ml Ulp1 protease carrying a C-terminal StrepII-tag in 2.5 bed volumes buffer TNT-Iz15 (25
782 mM Tris–HCl pH 8, 150 mM NaCl, 1 mM TCEP, 15 mM imidazole) overnight at 4°C. The
783 eluate was collected, retained cleavage products were washed off the beads with buffer G, and
784 all fractions were pooled. The combined eluate was diluted 1:3 in 25 mM Tris-HCl pH 8 + 0.1
785 mM TCEP, passed through a 0.22 µm filter, and further purified by anion exchange
786 chromatography using a 6 ml RESOURCE Q column (GE Healthcare) equilibrated in 95%
787 AEX-A (25 mM Tris–HCl pH 8, 25 mM NaCl, 0.1 mM TCEP) and 5% AEX-B (25 mM Tris–
788 HCl pH 8, 1 M NaCl, 0.1 mM TCEP). Proteins were eluted by applying a gradient from 5 to
789 50% AEX-B in 25 CV at 6 ml/min. The elution peak fractions corresponding to Grp170 were
790 pooled and 1 mM TCEP was added. After buffer exchange to HKT (50 mM HEPES-KOH pH
791 7.4, 150 mM KCl, 1 mM TCEP) and concentration using 30-kDa MWCO centrifugal filters,
792 the proteins were frozen in aliquots and stored at -80°C. BiP from *Drosophila melanogaster*
793 (UK2354) and human Hsp70 (UK2510; natural variant E110D) and Hsc70 (UK2511) were all
794 expressed as fusion proteins with an N-terminal His6-Smt3 and purified likewise.
795 DnaK (from *Escherichia coli*) with an N-terminal His6-Smt3 (UK2243) was expressed and
796 purified likewise, except that after anion exchange chromatography the pooled eluate was
797 adjusted to 500 mM NaCl and 40 mM imidazole. The eluate was then incubated with 1 ml Ni-
798 NTA agarose for 1 h rotating at 4°C (to remove traces of uncleaved protein). The beads were
799 then collected by centrifugation at 100 × *g* for 2 min and the supernatant was transferred to a
800 30-kDa MWCO centrifugal filter for buffer exchange to HKT and protein concentration.
801
802 <u>Nucleotide binding domains of BiP, Hsp70 and Hsc70 for crystallisation</u>
803
804 All NBDs were expressed as fusion proteins with a N-terminal His6-Smt3. The NBD of
805 hamster BiP (UK2039) was produced in M15 *E. coli* cells grown in LB medium containing 50
806 µg/ml kanamycin and 100 mg/ml ampicillin. The NBDs of human Hsp70 (UK2532; natural
807 variant E110D) and human Hsc70 (UK2533) were produced in *E. coli* BL21 T7 Express
808 lysY/Iq cells grown in LB medium containing 50 µg/ml kanamycin. The cells were grown at
809 37°C to OD$_{600 nm}$ 0.5, transferred to 22°C for 20 min, and expression was induced with 0.5 mM
810 IPTG. After incubation for 14 h at 22°C the cells were collected by centrifugation and
811 suspended in lysis buffer G (50 mM Tris-HCl pH 8, 500 mM NaCl, 20 mM imidazole)
812 containing protease inhibitors (1 mM PMSF, 2 µg/ml pepstatin, 8 µg/ml aprotinin, 2 µM
813 leupeptin), 1 mM MgCl$_2$, 0.1 mM TCEP, and 0.1 mg/ml DNaseI. The cells were lysed with an
814 EmulsiFlex-C3 high-pressure homogeniser and lysates were centrifuged for 30 min at 45,000
815 × *g* at 4°C. The cleared lysates were incubated with 1 ml Ni-NTA agarose beads per 1 l
816 expression culture for 30 min rotating at 4°C. The beads were then transferred to a 49-ml
817 gravity-flow column, washed in 2 CV lysis buffer G, 2 CV buffer H (50 mM Tris-HCl pH 8,
818 500 mM NaCl, 30 mM imidazole, 5 mM β-mercaptoethanol), 2 CV buffer I (50 mM Tris-HCl
819 pH 8, 300 mM NaCl, 10 mM imidazole, 5 mM β-mercaptoethanol), and with buffer I
820 supplemented sequentially with (i) 1 M NaCl, (ii) 10 mM MgCl$_2$ + 3 mM ATP + 0.01 mg/ml
821 RNaseA, or (iii) 0.5 M Tris–HCl pH 8 + 1 mM TCEP (2 CV each), followed by 2 CV buffer
822 TNT-Iz10 (25 mM Tris–HCl pH 8, 150 mM NaCl, 1 mM TCEP, 10 mM imidazole). Proteins
823 were eluted by on-column cleavage with 3.7 µg/ml Ulp1 protease carrying a C-terminal
824 StrepII-tag in 1 bed volume buffer TNT-Iz10 overnight at 4°C. The eluate was collected,
825 retained cleavage products were washed off the beads with buffer TNT-Iz10, and all fractions
826 were pooled. To remove bound nucleotide, the proteins were dialysed for 6 h against buffer J

827 (25 mM Tris-HCl pH 8, 150 mM NaCl, 5 mM EDTA, 5 mM β-mercaptoethanol), 16 h against
828 fresh buffer J, 6 h against buffer K (25 mM Tris-HCl pH 8, 100 mM NaCl, 5 mM β-
829 mercaptoethanol), and 16 h against fresh buffer K. The protein solutions were then diluted 1:2
830 with 25 mM Tris-Hcl pH 8 + 0.2 mM TCEP, filtered (0.22 µm filter), and applied to anion
831 exchange chromatography using a 6 ml RESOURCE Q column equilibrated in 100% AEX-A1
832 (25 mM Tris–HCl pH 8, 75 mM NaCl, 0.2 mM TCEP). The flow-through fractions were
833 collected and bound proteins were eluted by applying a gradient from 0 to 50% AEX-B2 (25
834 mM Tris–HCl pH 8, 1 M NaCl, 0.2 mM TCEP) in 25 CV at 5 ml/min. The fractions
835 corresponding to the NBD proteins were pooled and further purified. In case of the NBDs of
836 Hsp70 (UK2532) and Hsc70 (UK2533) the unbound material (flow-through of the loading
837 step) was used for further purification. The proteins were concentrated ,applied to gel-filtration
838 using a Superdex 75 prep grade HiLoad 16/60 column (GE Healthcare) equilibrated in buffer
839 K (10 mM Tris-HCl pH 8, 150 mM KCl, 0.2 mM TCEP), and proteins were eluted at 0.75
840 ml/min. The elution peak fractions were pooled, supplemented with 1 mM TCEP, and proteins
841 were concentrated in 10-kDa MWCO centrifugal filter to ∼1-1.5 mM. The protein preparations
842 were frozen in aliquots and stored at -80°C for crystallisation and functional experiments.
843
844 <u>Nucleotide binding domains (NBDs) of *Drosophila* BiP, DnaK and Kar2</u>
845
846 The NBDs were expressed as fusion proteins with a N-terminal His6-Smt3. The NBD of
847 *Drosophila* BiP (UK2534) was produced in M15 *E. coli* cells grown in LB medium containing
848 50 µg/ml kanamycin and 100 mg/ml ampicillin. The NBDs of DnaK (UK2531) and yeast Kar2
849 (UK2606) were produced in *E. coli* BL21 T7 Express lysY/Iq cells grown in LB medium
850 containing 50 µg/ml kanamycin. The cells were grown at 37°C to $OD_{600\ nm}$ 0.5, transferred to
851 22°C for 20 min, and expression was induced with 0.5 mM IPTG. After incubation for 14 h at
852 22°C, the cells were collected by centrifugation and suspended in lysis buffer E (50 mM Tris-
853 HCl pH 8, 500 mM NaCl, 20 mM imidazole, 10% glycerol) containing protease inhibitors (1
854 mM PMSF, 2 µg/ml pepstatin, 8 µg/ml aprotinin, 2 µM leupeptin), 1 mM $MgCl_2$, 0.1 mM
855 TCEP, and 0.1 mg/ml DNaseI. The cells were lysed with an EmulsiFlex-C3 high-pressure
856 homogeniser and lysates were centrifuged for 30 min at 45,000 × *g* at 4°C. The cleared lysates
857 were incubated with 1 ml Ni-NTA agarose beads per 1 l expression culture for 30 min rotating
858 at 4°C. The beads were then transferred to a 49-ml gravity-flow column, washed in 2 CV lysis
859 buffer G, 2 CV buffer H (50 mM Tris-HCl pH 8, 500 mM NaCl, 30 mM imidazole, 5 mM β-
860 mercaptoethanol), 2 CV buffer I (50 mM Tris-HCl pH 8, 300 mM NaCl, 10 mM imidazole, 5
861 mM β-mercaptoethanol) and with buffer I supplemented sequentially with (i) 1 M NaCl, (ii)
862 10 mM $MgCl_2$ + 3 mM ATP + 0.01 mg/ml RNaseA, or (iii) 0.5 M Tris–HCl pH 8 + 1 mM
863 TCEP (2 CV each), followed by 2 CV buffer TNT-Iz10 (25 mM Tris–HCl pH 8, 150 mM
864 NaCl, 1 mM TCEP, 10 mM imidazole). Proteins were eluted by on-column cleavage with 3.7
865 µg/ml Ulp1 protease carrying a C-terminal StrepII-tag in 1 bed volume buffer TNT-Iz10
866 overnight at 4°C. The eluate was collected, retained cleavage products were washed off the
867 beads with buffer TNT-Iz10, and all fractions were pooled. After buffer exchange to HKT (50
868 mM HEPES-KOH pH 7.4, 150 mM KCl, 1 mM TCEP) and concentration using 10-kDa
869 MWCO centrifugal filters, the proteins were frozen in aliquots and stored at -80°C for
870 functional experiments.
871
872 <u>BiP for oligomer crystallisation</u>
873
874 Chinese hamster BiP$^{T229A-V461F}$ (residues 28-549) was expressed as an N-terminal His6-Smt3-
875 tagged protein (UK2090). The purification protocol was the same as used for His6-Smt3-FICD

876 purification described in (Perera et al., 2019) with minor modifications. The protein was
877 expressed in M15 *E. coli* cells grown in LB medium supplemented with 100 µg/ml ampicillin
878 and 50 µg/ml kanamycin. After anion exchange chromatography the protein was exchanged
879 into 10 mM HEPES-KOH pH 7.4, 150 mM KCl, 2 mM MgCl$_2$, and 1 mM TCEP by gel
880 filtration and concentrated to 21 mg/ml.

882 For crystallisation, BiP and an equimolar amount of human FICD$^{L258D-H363A}$ [residues 104-445;
883 UK2093, purified as in (Perera et al., 2019)] were diluted to 150 µM with TNKM (10 mM
884 Tris-HCl pH 8.0, 100 mM NaCl, 50 mM KCl and 2 mM MgCl$_2$) and supplemented with 175
885 µM ATP. Note: FICD was excluded from the resulting crystals of oligomeric BiP (see below).

887 <u>Biotinylated J domains</u>

889 The J-domain of *E. coli* DnaJ (amino acids 1-72; UK2470) as well as the wildtype (UK1965;
890 J) and H422Q mutant (UK1966; J^{QPD}) J-domain of mammalian ERdj6 (amino acids 390-455)
891 were expressed with an AviTag-His6 sequence at the C-terminus in BL21 T7 Express lysY/Iq
892 cells grown in LB medium containing 50 µg/ml kanamycin. The cells were grown at 37°C to
893 OD$_{600\,nm}$ 0.5, transferred to 18°C for 20 min, and expression was induced with 0.5 mM IPTG.
894 The cells were incubated for 16 h at 18°C during which the recombinant proteins were
895 biotinylated on the AviTag to sufficient degree by the endogenous *E. coli* BirA biotin ligase.
896 Afterwards, the cells were collected by centrifugation and lysed in buffer G (50 mM Tris-HCl
897 pH 8, 500 mM NaCl, 20 mM imidazole) containing protease inhibitors (1 mM PMSF, 2 µg/ml
898 pepstatin, 8 µg/ml aprotinin, 2 µM leupeptin), 1 mM MgCl$_2$, 0.1 mM TCEP, 0.1 mg/ml DNaseI,
899 and 0.02 mg/ml RNaseA using an EmulsiFlex-C3 high-pressure homogeniser. The lysates were
900 cleared for 30 min at 45,000 × *g* at 4°C and the supernatants were incubated with 1 ml Ni-NTA
901 agarose beads per 1 l expression culture for 2 h rotating at 4°C. The beads were then transferred
902 to a 49-ml gravity-flow column, washed with 1 CV buffer I (50 mM Tris-HCl pH 8, 300 mM
903 NaCl, 10 mM imidazole, 5 mM β-mercaptoethanol) and with buffer I supplemented
904 sequentially with (i) 1 M NaCl, (ii) 10 mM MgCl$_2$ + 3 mM ATP, or (iii) 0.5 M Tris–HCl pH 8
905 + 1 mM TCEP (2 CV each), followed by 2 CV buffer I containing 35 mM imidazole. Proteins
906 were eluted in buffer J (50 mM Tris-HCl pH 8, 300 mM NaCl, 250 mM imidazole) and dialysed
907 against TNM (50 mM Tris-HCl pH 8, 150 mM NaCl, 2 mM MgCl$_2$) for 16 h at 4°C and for
908 further 6 h against fresh TNM. The protein solutions were frozen in aliquots and stored at -
909 80°C for Bio-Layer interferometry experiments.

911 **X-ray crystallography**

913 Concentrated NBD protein preparations (see above) of hamster BiP (UK2039), human Hsp70
914 (UK2532), and human Hsc70 (UK2533) were adjusted to ~50 mg/ml. The preparations were
915 supplemented with an additional 7 mM CaCl$_2$ and 2 mM ADP. Crystallisation of NBDs was
916 performed in 96-well sitting drop plates by combining 200 nl protein solution with 200 nl
917 reservoir solution and equilibration at 20°C against 70 µl reservoir solution. Crystallisation of
918 lid-truncated BiP oligomers was achieved by mixing 100 nl of protein solution and 100 nl
919 reservoir solution. Diffraction quality crystals grew in the following solutions: BiP(NBD) —
920 26% PEG6000, 0.2M CaCl$_2$, 0.1M NaOAc pH 5; Hsp70(NBD) — 10% PEG8000, 0.1 M Tris
921 pH 8.4, 0.2 M CaCl$_2$; Hsc70(NBD) — 24% PEG3350, 0.2M CaOAc; apo BiP oligomer —
922 20% PEG3350, 0.1 M Bis-Tris Propane pH 7.5, 0.2 M Na$_3$Citrate; ADP-bound BiP oligomer
923 — 20% PEG3350, 0.2 M K$_3$Citrate. Crystals were soaked in cryosolution [the well solutions
924 containing additional 25% (v/v) glycerol] and snap frozen in liquid nitrogen. Diffraction data
925 were collected at the Diamond Light Source beamlines i03, i04, and i24 (Diamond Light

Source, United Kingdom; see Table S1) and processed by the XIA2 pipeline (Winter, 2010) implementing Mosflm (Battye et al., 2011) or XDS (Kabsch, 2010) for indexing and integration, Pointless (Evans, 2011) for space group determination, and Aimless (Winn et al., 2011), for scaling and merging. All structures were solved by molecular replacement in Phaser (McCoy et al., 2007). NBD datasets were solved by using BiP nucleotide binding domain (PDB 3IUC) as the search model. BiP oligomer structures were solved by searching for an ensemble of apo BiP's NBD and SBD, taken from PDB 6HAB. Manual model building was carried out in COOT (Emsley et al., 2010) and further refinements were performed in refmac5 (Winn et al., 2001) and phenix.refine (Liebschner et al., 2019). The final refinement statistics are summarised in Table S1. The structural graphs were generated with UCSF Chimera (Pettersen et al., 2004) and Pymol (version 1.3 educational). CheckMyMetal (Zheng et al., 2017) has been used for metal validation. The polder-maps in Figure 6-figure supplement 1A were calculated using phenix.polder (Liebschner et al., 2017) by omitting ADP, Ca^{2+} and Ca^{2+}-coordinated water molecules.

NADH ATPase assay

BiP (UK173), J (UK1965) and J^{QPD} (UK1966) proteins were diluted from concentrated stocks and exposed to ATP and β-NADH to start the reactions. Proteins were used at final concentrations as indicated. The reactions were performed in HK solution (50 mM HEPES-KOH pH 7.4, 100 mM KCl) containing 10 mM $MgCl_2$, 0.05% Triton X-100, 1 mM TCEP. The reactions also contained 4 mM ATP, 3 mM Phospho(enol)pyruvic acid (PEP; Sigma, P0564), 0.25 mM β-NADH (Sigma, N8129), and pyruvate kinase/lactic dehydrogenase enzyme mix (diluted final 1:45; Sigma, P0294). Where indicated 3 mM $CaCl_2$ was present. The reactions were carried out in a final volume of 110 µl in 384-well microplates (µClear ; Grainer bio-one, 781096) and β-NADH absorbance at 340 nm (A_{340}) was measured over time at 25°C with a Clariostar plate reader (BMG Labtech). Linear regression analysis was performed with Prism 8 (GraphPad) and the ATP hydrolysis activity were calculated using the molar extinction coefficient of β-NADH ($\varepsilon = 6220$ M^{-1} cm^{-1}).

Malachite green ATPase assay

Malachite green (MG) reaction solution was prepared freshly by combining stock solutions of MG dye (0.111% malachite green, 6 N sulphuric acid), 7.5% ammonium molybdate, and 11% Tween 20 in a 5:1.25:0.1 ratio. Samples of BiP protein (UK173) at 5 µM were prepared in HK solution containing 3 mM $MgCl_2$ and 3 mM ATP in a final volume of 20 µl. Where indicated ADP and $CaCl_2$ was added. The samples were incubated for 1.5 h at 26°C. Afterwards, 15 µl of each sample were diluted with 135 µl water on a 96-well plate, mixed with 50 µl MG reaction solution and incubated for 2 min at room temperature. Twenty µl of a 34% sodium citrate solution were added to each well. After further 30 min incubation at room temperature the absorbance at 623 nm (A_{623}) was measured with a plate reader (SpectraMax, Molecular Devices). Standard curves from serial dilutions of KH_2PO_4 served as a reference to calculate the specific ATPase activity.

Nucleotide binding assays

Nucleotide release and binding measurements were performed using the fluorescent nucleotide analogues MABA-ADP (Jena Bioscience, NU-893-MNT) and MABA-ATP (Jena Bioscience, NU-806-MNT) carrying a MANT moiety whose fluorescence increases upon binding to

Hsp70s (Theyssen et al., 1996). The measurements were started by adding 55 µl of solution A to 5 µl of solution B (specified below) in a quartz cuvette (Hellma Analytics) and fluorescence (excitation 360 nm, emission 420 nm) was detected over time with a fluorescence spectrometer (Perkin Elmer LS55) at 26°C. All solutions contained 50 mM HEPES-KOH pH 7.4, 100 mM KCl.

To measure nucleotide release, 1.42 µM fluorescent nucleotide analogues were incubated with 1.42 µM proteins in solution A for at least 1 h at 26°C to allow for complex formation (binding phase). Solution B contained assay buffer with 18 mM MgATP. Where specified, 15.6 µM Grp170 were added to solution B. The final concentrations after mixing (release phase) were 1.3 µM for each protein, 1.3 µM fluorescent nucleotides, and 1.5 mM MgATP. The solutions contained $MgCl_2$ and $CaCl_2$ where indicated (final concentrations are stated on the figures and in figure legends). For Ca^{2+} titration experiments, $CaCl_2$ was present in solution A and final $[CaCl_2]$ are plotted on the graphs and were used to calculate IC_{50} values. The dissociation rate constants (k_{off}) were determined by fitting the data to a one phase exponential function using Prism 8.4 (GraphPad). In experiments involving cytoplasmic Hsp70s all solutions contained 0.2 mM TCEP (Figure 5A, Figure 6C, Figure 6-figure supplement 2A).

The association rate constants (Figure 3C) were determined by combining nucleotide-free BiP (UK173) or BiP^{T229A} (UK838) proteins (in solution A) with MABA-ADP or MABA-ATP (in solution B) at the start of the measurement. Solutions A and B contained either 1 mM $MgCl_2$ or $CaCl_2$. Each association rate was calculated from six individual measurements, covering a final protein concentration range from 1.3 µM to 7.8 µM. For that, the data were fitted to a one phase exponential function and the observed rates (k_{obs}) were plotted against the protein concentration to calculate association rate constants (k_{on}) with the equation $k_{obs} = k_{on}[\text{protein}] + k_{off}$ using the dissociation rate constants (k_{off}) determined separately under the same conditions.

Bio-Layer interferometry (BLI)

BLI experiments were performed on the FortéBio Octet RED96 System (Pall FortéBio) in buffer solution containing 50 mM HEPES-KOH pH 7.4, 100 mM KCl, 0.2 mM TCEP, and 0.05% Triton X-100 (HKTTx). Nucleotide and divalent cations were added as indicated. Streptavidin (SA)-coated biosensors (Pall FortéBio) were hydrated in HKTTx solution for at least 10 min prior to use. Experiments were conducted at 28°C and 700 rpm shake speed and binding signals were recorded at an acquisition rate of 10 Hz. BLI reactions were prepared in 200 µl volumes in 96-well microplates (greiner bio-one, 655209). The following assay steps were performed: After an initial equilibration step in HKTTx solution (I), JDPs (J, UK1965 or J^{QPD}, UK1966) carrying a biotinylated Avi-tag (each at 5 µM in HKTTx) were loaded until a binding signal of ~0.4 nm was reached. After a brief wash step in assay solution (III) the binding sites on the sensors were saturated with P15 peptide (ALLLSAPRRGAGKK, biotinylated on the C-terminal lysine; custom synthesised by GenScript, Piscataway, NJ) solubilised at 100 nM in HKTTx solution (IV). The sensors were then washed in HKTTx until a stable baseline signal was established (V). Association of BiP or other Hsp70s was performed in HKTTx solution containing 3 mM $MgCl_2$, 1.5 mM ATP and the indicated proteins at 5 µM (VI). To allow for dissociation, the sensors were transferred to protein-free assay solution with variable components as indicated (VII). The data were processed in Prism 8.4 (GraphPad) and dissociation rate constants were obtained by fitting to a one phase exponential function. When DnaK was analysed (Figure 5C), a JDP containing the J-domain of DnaJ was immobilised (UK2470).

Differential scanning fluorimetry (DSF)

DSF measurements were performed on a Bio-Rad CFX96 Touch Real-Time PCR Detection System in 96-well plates (Bio-Rad Hard-Shell, #HSP9601) sealed with transparent adhesive film (Bio-Rad Microseal 'B' Adhessive Sealer, #MSB1001). Samples were prepared in a volume of 25 µl. The solutions contained 50 mM HEPES–KOH pH 7.4, 100 mM KCl, 1 mM TCEP and SYPRO orange protein gel stain at a 1:500 dilution of the manufacturer's stock (Invitrogen, S6651). The samples also contained 5 µM NBD protein, 4 mM ADP, and 6 mM $MgCl_2$ or $CaCl_2$ as indicated. The plates were centrifuged for 1 min at $150 \times g$ before the experiment. Temperature scanning was performed in 0.5°C intervals from 20 to 95°C and SYPRO orange fluorescence was detected. The data were then analysed in Prism 8.4 (GraphPad) and the melting temperature (T_m) was determined as the temperature corresponding to the global minimum of the negative first derivatives of the melt curves.

Size-exclusion chromatography (SEC)

Samples for analytical SEC were prepared in SEC buffer (50 mM HEPES-KOH pH 7.4, 150 mM KCl, 10 mM $MgCl_2$) in a final volume of 25 µl. The samples were incubated for at least 20 min at 25°C before 10 µl were injected onto a SEC-3 HPLC column (300 Å pore size; Agilent Technologies, Santa Clara, CA) equilibrated with SEC buffer. The runs were performed at a flow rate of 0.3 ml/min at 26°C and peptide bond absorbance at 230 nm (A_{230}) was detected and plotted against the elution time. A gel filtration standard (Bio-Rad, 151–1901) was applied as a size reference and the elution peaks of Thyroglobulin (670 kDa), γ-globulin (158 kDa), Ovalbumin (44 kDa), and Myoglobulin (17 kDa) are indicated.

In the experiment shown in Figure 7C, the samples contained 40 µM BiP protein (UK173) and 1 mM ADP and the samples were incubated for 20 min at 24°C before SEC analysis. Where indicated, 36 ng/µl SubA protease was added during the incubation period.

For the experiment shown in Figure 7D, BiP at 50 µM was incubated for 6 h at 24°C with 1 mM ADP and 1.3 µM fluorescently labelled NR peptide (NRLLLTG carrying a fluorescein moiety at the N-terminus, custom synthesised by GenScript at >95% purity) (Yang et al., 2017). Afterwards, the samples were incubated without or with SubA protease (36 ng/µl) for 30 min before SEC analysis. Where indicated, 5 mM ATP was added 10 min before injection onto the column. The final concentration of BiP in the samples was 45 µM. The fluorescein fluorescence signal (excitation 495nm; emission 520 nm) of the peptide was recorded separately during the SEC runs.

For the experiment shown in Figure 7-figure supplement 2, untreated BiP protein or SubA-treated, purified BiP oligomers (both at 20 µM) were incubated without or with 4 mM ATP in SEC buffer solution at 26°C as indicated. The BiP oligomers had been thawed from frozen stocks before the experiment.

***t*-tests**

Unpaired (degrees of freedom = total sample size minus 2), parametric (assuming equal variance), *t*-tests were applied where indicated using GraphPad Prism 8.

References

1. Alvarez, J., and Montero, M. (2002). Measuring [Ca2+] in the endoplasmic reticulum with aequorin. Cell Calcium *32*, 251-260.

2. Amin-Wetzel, N., Neidhardt, L., Yan, Y., Mayer, M.P., and Ron, D. (2019). Unstructured regions in IRE1alpha specify BiP-mediated destabilisation of the luminal domain dimer and repression of the UPR. Elife *8*.

3. Amin-Wetzel, N., Saunders, R.A., Kamphuis, M.J., Rato, C., Preissler, S., Harding, H.P., and Ron, D. (2017). A J-Protein Co-chaperone Recruits BiP to Monomerize IRE1 and Repress the Unfolded Protein Response. Cell *171*, 1625-1637 e1613.

4. Avezov, E., Cross, B.C., Kaminski Schierle, G.S., Winters, M., Harding, H.P., Melo, E.P., Kaminski, C.F., and Ron, D. (2013). Lifetime imaging of a fluorescent protein sensor reveals surprising stability of ER thiol redox. J Cell Biol *201*, 337-349.

5. Avezov, E., Konno, T., Zyryanova, A., Chen, W., Laine, R., Crespillo-Casado, A., Melo, E.P., Ushioda, R., Nagata, K., Kaminski, C.F.*, et al.* (2015). Retarded PDI diffusion and a reductive shift in poise of the calcium depleted endoplasmic reticulum. BMC Biol *13*, 2.

6. Baksh, S., and Michalak, M. (1991). Expression of calreticulin in Escherichia coli and identification of its Ca2+ binding domains. J Biol Chem *266*, 21458-21465.

7. Bakunts, A., Orsi, A., Vitale, M., Cattaneo, A., Lari, F., Tade, L., Sitia, R., Raimondi, A., Bachi, A., and van Anken, E. (2017). Ratiometric sensing of BiP-client versus BiP levels by the unfolded protein response determines its signaling amplitude. Elife *6*.

8. Battye, T.G., Kontogiannis, L., Johnson, O., Powell, H.R., and Leslie, A.G. (2011). iMOSFLM: a new graphical interface for diffraction-image processing with MOSFLM. Acta Crystallogr D Biol Crystallogr *67*, 271-281.

9. Behnke, J., Feige, M.J., and Hendershot, L.M. (2015). BiP and its nucleotide exchange factors Grp170 and Sil1: mechanisms of action and biological functions. J Mol Biol *427*, 1589-1608.

10. Berridge, M.J., Lipp, P., and Bootman, M.D. (2000). The versatility and universality of calcium signalling. Nat Rev Mol Cell Biol *1*, 11-21.

11. Bertolotti, A., Zhang, Y., Hendershot, L.M., Harding, H.P., and Ron, D. (2000). Dynamic interaction of BiP and ER stress transducers in the unfolded-protein response. Nat Cell Biol *2*, 326-332.

12. Blond-Elguindi, S., Fourie, A.M., Sambrook, J.F., and Gething, M.J. (1993). Peptide-dependent stimulation of the ATPase activity of the molecular chaperone BiP is the result of conversion of oligomers to active monomers. J Biol Chem *268*, 12730-12735.

13. Bonifacino, J.S., Cosson, P., and Klausner, R.D. (1990). Colocalized transmembrane determinants for ER degradation and subunit assembly explain the intracellular fate of TCR chains. Cell *63*, 503-513.

14. Bonifacino, J.S., Cosson, P., Shah, N., and Klausner, R.D. (1991). Role of potentially charged transmembrane residues in targeting proteins for retention and degradation within the endoplasmic reticulum. EMBO J *10*, 2783-2793.

15. Bygrave, F.L., and Benedetti, A. (1996). What is the concentration of calcium ions in the endoplasmic reticulum? Cell Calcium *19*, 547-551.

16. Carreras-Sureda, A., Pihan, P., and Hetz, C. (2018). Calcium signaling at the endoplasmic reticulum: fine-tuning stress responses. Cell Calcium *70*, 24-31.

17. Chen, D., Gibson, E.S., and Kennedy, M.J. (2013). A light-triggered protein secretion system. J Cell Biol *201*, 631-640.

1123 18. Cooper, G.R., Brostrom, C.O., and Brostrom, M.A. (1997). Analysis of the
1124   endoplasmic reticular Ca2+ requirement for alpha1-antitrypsin processing and
1125   transport competence. Biochem J *325 (Pt 3)*, 601-608.
1126 19. Corbett, E.F., Oikawa, K., Francois, P., Tessier, D.C., Kay, C., Bergeron, J.J., Thomas,
1127   D.Y., Krause, K.H., and Michalak, M. (1999). Ca2+ regulation of interactions between
1128   endoplasmic reticulum chaperones. J Biol Chem *274*, 6203-6211.
1129 20. Denis, V., and Cyert, M.S. (2002). Internal Ca(2+) release in yeast is triggered by
1130   hypertonic shock and mediated by a TRP channel homologue. J Cell Biol *156*, 29-34.
1131 21. Depaoli, M.R., Karsten, F., Madreiter-Sokolowski, C.T., Klec, C., Gottschalk, B.,
1132   Bischof, H., Eroglu, E., Waldeck-Weiermair, M., Simmen, T., Graier, W.F.*, et al.*
1133   (2018). Real-Time Imaging of Mitochondrial ATP Dynamics Reveals the Metabolic
1134   Setting of Single Cells. Cell Rep *25*, 501-512 e503.
1135 22. Dierks, T., Volkmer, J., Schlenstedt, G., Jung, C., Sandholzer, U., Zachmann, K.,
1136   Schlotterhose, P., Neifer, K., Schmidt, B., and Zimmermann, R. (1996). A microsomal
1137   ATP-binding protein involved in efficient protein transport into the mammalian
1138   endoplasmic reticulum. EMBO J *15*, 6931-6942.
1139 23. Dupont, G., Combettes, L., Bird, G.S., and Putney, J.W. (2011). Calcium oscillations.
1140   Cold Spring Harb Perspect Biol *3*.
1141 24. Emsley, P., Lohkamp, B., Scott, W.G., and Cowtan, K. (2010). Features and
1142   development of Coot. Acta Crystallogr D Biol Crystallogr *66*, 486-501.
1143 25. Evans, P.R. (2011). An introduction to data reduction: space-group determination,
1144   scaling and intensity statistics. Acta Crystallogr D Biol Crystallogr *67*, 282-292.
1145 26. Fass, D., Blacklow, S., Kim, P.S., and Berger, J.M. (1997). Molecular basis of familial
1146   hypercholesterolaemia from structure of LDL receptor module. Nature *388*, 691-693.
1147 27. Gaut, J.R., and Hendershot, L.M. (1993). Mutations within the nucleotide binding site
1148   of immunoglobulin-binding protein inhibit ATPase activity and interfere with release
1149   of immunoglobulin heavy chain. J Biol Chem *268*, 7248-7255.
1150 28. Groenendyk, J., Peng, Z., Dudek, E., Fan, X., Mizianty, M.J., Dufey, E., Urra, H.,
1151   Sepulveda, D., Rojas-Rivera, D., Lim, Y.*, et al.* (2014). Interplay between the
1152   oxidoreductase PDIA6 and microRNA-322 controls the response to disrupted
1153   endoplasmic reticulum calcium homeostasis. Sci Signal *7*, ra54.
1154 29. Guest, P.C., Bailyes, E.M., and Hutton, J.C. (1997). Endoplasmic reticulum Ca2+ is
1155   important for the proteolytic processing and intracellular transport of proinsulin in the
1156   pancreatic beta-cell. Biochem J *323 (Pt 2)*, 445-450.
1157 30. Halachmi, D., and Eilam, Y. (1989). Cytosolic and vacuolar Ca2+ concentrations in
1158   yeast cells measured with the Ca2+-sensitive fluorescence dye indo-1. FEBS Lett *256*,
1159   55-61.
1160 31. Harding, H.P., Zhang, Y., and Ron, D. (1999). Protein translation and folding are
1161   coupled by an endoplasmic-reticulum-resident kinase. Nature *397*, 271-274.
1162 32. Harding, H.P., Zyryanova, A.F., and Ron, D. (2012). Uncoupling proteostasis and
1163   development in vitro with a small molecule inhibitor of the pancreatic endoplasmic
1164   reticulum kinase, PERK. The Journal of biological chemistry.
1165 33. Hirschberg, K., Miller, C.M., Ellenberg, J., Presley, J.F., Siggia, E.D., Phair, R.D., and
1166   Lippincott-Schwartz, J. (1998). Kinetic analysis of secretory protein traffic and
1167   characterization of golgi to plasma membrane transport intermediates in living cells. J
1168   Cell Biol *143*, 1485-1503.
1169 34. Kabsch, W. (2010). Xds. Acta Crystallogr D Biol Crystallogr *66*, 125-132.
1170 35. Karagoz, G.E., Acosta-Alvear, D., and Walter, P. (2019). The Unfolded Protein
1171   Response: Detecting and Responding to Fluctuations in the Protein-Folding Capacity
1172   of the Endoplasmic Reticulum. Cold Spring Harb Perspect Biol *11*.

1173 36. Kassenbrock, C.K., and Kelly, R.B. (1989). Interaction of heavy chain binding protein
1174   (BiP/GRP78) with adenine nucleotides. EMBO J *8*, 1461-1467.
1175 37. Kozutsumi, Y., Segal, M., Normington, K., Gething, M.J., and Sambrook, J. (1988).
1176   The presence of malfolded proteins in the endoplasmic reticulum signals the induction
1177   of glucose-regulated proteins. Nature *332*, 462-464.
1178 38. Kurtoglu, M., Gao, N., Shang, J., Maher, J.C., Lehrman, M.A., Wangpaichitr, M.,
1179   Savaraj, N., Lane, A.N., and Lampidis, T.J. (2007). Under normoxia, 2-deoxy-D-
1180   glucose elicits cell death in select tumor types not by inhibition of glycolysis but by
1181   interfering with N-linked glycosylation. Mol Cancer Ther *6*, 3049-3058.
1182 39. Lamb, H.K., Mee, C., Xu, W., Liu, L., Blond, S., Cooper, A., Charles, I.G., and
1183   Hawkins, A.R. (2006). The affinity of a major Ca2+ binding site on GRP78 is
1184   differentially enhanced by ADP and ATP. J Biol Chem *281*, 8796-8805.
1185 40. Lebeche, D., Lucero, H.A., and Kaminer, B. (1994). Calcium binding properties of
1186   rabbit liver protein disulfide isomerase. Biochem Biophys Res Commun *202*, 556-561.
1187 41. Liebschner, D., Afonine, P.V., Baker, M.L., Bunkoczi, G., Chen, V.B., Croll, T.I.,
1188   Hintze, B., Hung, L.W., Jain, S., McCoy, A.J.*, et al.* (2019). Macromolecular structure
1189   determination using X-rays, neutrons and electrons: recent developments in Phenix.
1190   Acta Crystallogr D Struct Biol *75*, 861-877.
1191 42. Liebschner, D., Afonine, P.V., Moriarty, N.W., Poon, B.K., Sobolev, O.V., Terwilliger,
1192   T.C., and Adams, P.D. (2017). Polder maps: improving OMIT maps by excluding bulk
1193   solvent. Acta Crystallographica Section D *73*, 148-157.
1194 43. Lievremont, J.P., Rizzuto, R., Hendershot, L., and Meldolesi, J. (1997). BiP, a major
1195   chaperone protein of the endoplasmic reticulum lumen, plays a direct and important
1196   role in the storage of the rapidly exchanging pool of Ca2+. J Biol Chem *272*, 30873-
1197   30879.
1198 44. Lippincott-Schwartz, J., Yuan, L.C., Bonifacino, J.S., and Klausner, R.D. (1989). Rapid
1199   redistribution of Golgi proteins into the ER in cells treated with brefeldin A: evidence
1200   for membrane cycling from Golgi to ER. Cell *56*, 801-813.
1201 45. Lodish, H.F., and Kong, N. (1990). Perturbation of cellular calcium blocks exit of
1202   secretory proteins from the rough endoplasmic reticulum. J Biol Chem *265*, 10893-
1203   10899.
1204 46. Lodish, H.F., Kong, N., and Wikstrom, L. (1992). Calcium is required for folding of
1205   newly made subunits of the asialoglycoprotein receptor within the endoplasmic
1206   reticulum. J Biol Chem *267*, 12753-12760.
1207 47. Lucero, H.A., Lebeche, D., and Kaminer, B. (1994). ERcalcistorin/protein disulfide
1208   isomerase (PDI). Sequence determination and expression of a cDNA clone encoding a
1209   calcium storage protein with PDI activity from endoplasmic reticulum of the sea urchin
1210   egg. J Biol Chem *269*, 23112-23119.
1211 48. Macer, D.R., and Koch, G.L. (1988). Identification of a set of calcium-binding proteins
1212   in reticuloplasm, the luminal content of the endoplasmic reticulum. J Cell Sci *91 (Pt
1213   1)*, 61-70.
1214 49. Mayer, M., Reinstein, J., and Buchner, J. (2003). Modulation of the ATPase cycle of
1215   BiP by peptides and proteins. J Mol Biol *330*, 137-144.
1216 50. McCoy, A.J., Grosse-Kunstleve, R.W., Adams, P.D., Winn, M.D., Storoni, L.C., and
1217   Read, R.J. (2007). Phaser crystallographic software. J Appl Crystallogr *40*, 658-674.
1218 51. Meldolesi, J., and Pozzan, T. (1998). The endoplasmic reticulum Ca2+ store: a view
1219   from the lumen. Trends Biochem Sci *23*, 10-14.
1220 52. Misselwitz, B., Staeck, O., and Rapoport, T.A. (1998). J proteins catalytically activate
1221   Hsp70 molecules to trap a wide range of peptide sequences. Mol Cell *2*, 593-603.

53. Munro, S., and Pelham, H.R. (1986). An Hsp70-like protein in the ER: identity with the 78 kd glucose-regulated protein and immunoglobulin heavy chain binding protein. Cell *46*, 291-300.

54. Paton, A.W., Beddoe, T., Thorpe, C.M., Whisstock, J.C., Wilce, M.C., Rossjohn, J., Talbot, U.M., and Paton, J.C. (2006). AB5 subtilase cytotoxin inactivates the endoplasmic reticulum chaperone BiP. Nature *443*, 548-552.

55. Pena, F., Jansens, A., van Zadelhoff, G., and Braakman, I. (2010). Calcium as a crucial cofactor for low density lipoprotein receptor folding in the endoplasmic reticulum. J Biol Chem *285*, 8656-8664.

56. Perera, L.A., Rato, C., Yan, Y., Neidhardt, L., McLaughlin, S.H., Read, R.J., Preissler, S., and Ron, D. (2019). An oligomeric state-dependent switch in the ER enzyme FICD regulates AMPylation and deAMPylation of BiP. EMBO J, e102177.

57. Pettersen, E.F., Goddard, T.D., Huang, C.C., Couch, G.S., Greenblatt, D.M., Meng, E.C., and Ferrin, T.E. (2004). UCSF Chimera--a visualization system for exploratory research and analysis. J Comput Chem *25*, 1605-1612.

58. Polier, S., Dragovic, Z., Hartl, F.U., and Bracher, A. (2008). Structural basis for the cooperation of Hsp70 and Hsp110 chaperones in protein folding. Cell *133*, 1068-1079.

59. Preissler, S., Chambers, J.E., Crespillo-Casado, A., Avezov, E., Miranda, E., Perez, J., Hendershot, L.M., Harding, H.P., and Ron, D. (2015). Physiological modulation of BiP activity by trans-protomer engagement of the interdomain linker. Elife *4*, e08961.

60. Preissler, S., Rohland, L., Yan, Y., Chen, R., Read, R.J., and Ron, D. (2017). AMPylation targets the rate-limiting step of BiP's ATPase cycle for its functional inactivation. Elife *6*.

61. Raffaello, A., Mammucari, C., Gherardi, G., and Rizzuto, R. (2016). Calcium at the Center of Cell Signaling: Interplay between Endoplasmic Reticulum, Mitochondria, and Lysosomes. Trends Biochem Sci *41*, 1035-1049.

62. Sagara, Y., and Inesi, G. (1991). Inhibition of the sarcoplasmic reticulum Ca2+ transport ATPase by thapsigargin at subnanomolar concentrations. J Biol Chem *266*, 13503-13506.

63. Sans, M.D., Kimball, S.R., and Williams, J.A. (2002). Effect of CCK and intracellular calcium to regulate eIF2B and protein synthesis in rat pancreatic acinar cells. Am J Physiol Gastrointest Liver Physiol *282*, G267-276.

64. Satpute-Krishnan, P., Ajinkya, M., Bhat, S., Itakura, E., Hegde, R.S., and Lippincott-Schwartz, J. (2014). ER stress-induced clearance of misfolded GPI-anchored proteins via the secretory pathway. Cell *158*, 522-533.

65. Sekijima, Y., Wiseman, R.L., Matteson, J., Hammarstrom, P., Miller, S.R., Sawkar, A.R., Balch, W.E., and Kelly, J.W. (2005). The biological and chemical basis for tissue-selective amyloid disease. Cell *121*, 73-85.

66. Sekine, Y., Zyryanova, A., Crespillo-Casado, A., Amin-Wetzel, N., Harding, H.P., and Ron, D. (2016). Paradoxical Sensitivity to an Integrated Stress Response Blocking Mutation in Vanishing White Matter Cells. PLoS One *11*, e0166278.

67. Shen, J., Chen, X., Hendershot, L., and Prywes, R. (2002). ER stress regulation of ATF6 localization by dissociation of BiP/GRP78 binding and unmasking of Golgi localization signals. Dev Cell *3*, 99-111.

68. Solovyova, N., and Verkhratsky, A. (2002). Monitoring of free calcium in the neuronal endoplasmic reticulum: an overview of modern approaches. J Neurosci Methods *122*, 1-12.

69. Strayle, J., Pozzan, T., and Rudolph, H.K. (1999). Steady-state free Ca(2+) in the yeast endoplasmic reticulum reaches only 10 microM and is mainly controlled by the secretory pathway pump pmr1. EMBO J *18*, 4733-4743.

70. Suzuki, C.K., Bonifacino, J.S., Lin, A.Y., Davis, M.M., and Klausner, R.D. (1991). Regulating the retention of T-cell receptor alpha chain variants within the endoplasmic reticulum: Ca(2+)-dependent association with BiP. J Cell Biol *114*, 189-205.

71. Thastrup, O., Cullen, P.J., Drobak, B.K., Hanley, M.R., and Dawson, A.P. (1990). Thapsigargin, a tumor promoter, discharges intracellular Ca2+ stores by specific inhibition of the endoplasmic reticulum Ca2(+)-ATPase. Proc Natl Acad Sci U S A *87*, 2466-2470.

72. Theyssen, H., Schuster, H.P., Packschies, L., Bukau, B., and Reinstein, J. (1996). The second step of ATP binding to DnaK induces peptide release. J Mol Biol *263*, 657-670.

73. Thomas, A.P., Bird, G.S., Hajnoczky, G., Robb-Gaspers, L.D., and Putney, J.W., Jr. (1996). Spatial and temporal aspects of cellular calcium signaling. Faseb J *10*, 1505-1517.

74. Van, P.N., Peter, F., and Soling, H.D. (1989). Four intracisternal calcium-binding glycoproteins from rat liver microsomes with high affinity for calcium. No indication for calsequestrin-like proteins in inositol 1,4,5-trisphosphate-sensitive calcium sequestering rat liver vesicles. J Biol Chem *264*, 17494-17501.

75. Vishnu, N., Jadoon Khan, M., Karsten, F., Groschner, L.N., Waldeck-Weiermair, M., Rost, R., Hallstrom, S., Imamura, H., Graier, W.F., and Malli, R. (2014). ATP increases within the lumen of the endoplasmic reticulum upon intracellular Ca2+ release. Mol Biol Cell *25*, 368-379.

76. Wada, I., Rindress, D., Cameron, P.H., Ou, W.J., Doherty, J.J., 2nd, Louvard, D., Bell, A.W., Dignard, D., Thomas, D.Y., and Bergeron, J.J. (1991). SSR alpha and associated calnexin are major calcium binding proteins of the endoplasmic reticulum membrane. J Biol Chem *266*, 19599-19610.

77. Wall, D., Zylicz, M., and Georgopoulos, C. (1994). The NH2-terminal 108 amino acids of the Escherichia coli DnaJ protein stimulate the ATPase activity of DnaK and are sufficient for lambda replication. J Biol Chem *269*, 5446-5451.

78. Walter, P., and Ron, D. (2011). The unfolded protein response: from stress pathway to homeostatic regulation. Science *334*, 1081-1086.

79. Wei, J., and Hendershot, L.M. (1995). Characterization of the nucleotide binding properties and ATPase activity of recombinant hamster BiP purified from bacteria. J Biol Chem *270*, 26670-26676.

80. Weitzmann, A., Baldes, C., Dudek, J., and Zimmermann, R. (2007). The heat shock protein 70 molecular chaperone network in the pancreatic endoplasmic reticulum - a quantitative approach. Febs J *274*, 5175-5187.

81. Welch, W.J., Garrels, J.I., Thomas, G.P., Lin, J.J., and Feramisco, J.R. (1983). Biochemical characterization of the mammalian stress proteins and identification of two stress proteins as glucose- and Ca2+-ionophore-regulated proteins. J Biol Chem *258*, 7102-7111.

82. Winn, M.D., Ballard, C.C., Cowtan, K.D., Dodson, E.J., Emsley, P., Evans, P.R., Keegan, R.M., Krissinel, E.B., Leslie, A.G.W., McCoy, A.*, et al.* (2011). Overview of the CCP4 suite and current developments. Acta Crystallographica Section D *67*, 235-242.

83. Winn, M.D., Isupov, M.N., and Murshudov, G.N. (2001). Use of TLS parameters to model anisotropic displacements in macromolecular refinement. Acta Crystallogr D Biol Crystallogr *57*, 122-133.

84. Winter, G. (2010). xia2: an expert system for macromolecular crystallography data reduction. Journal of Applied Crystallography *43*, 186-190.

85. Wisniewska, M., Karlberg, T., Lehtio, L., Johansson, I., Kotenyova, T., Moche, M., and Schuler, H. (2010). Crystal structures of the ATPase domains of four human Hsp70

isoforms: HSPA1L/Hsp70-hom, HSPA2/Hsp70-2, HSPA6/Hsp70B', and HSPA5/BiP/GRP78. PLoS One *5*, e8625.

86. Wong, W.L., Brostrom, M.A., Kuznetsov, G., Gmitter-Yellen, D., and Brostrom, C.O. (1993). Inhibition of protein synthesis and early protein processing by thapsigargin in cultured cells. Biochem J *289 (Pt 1)*, 71-79.

87. Wu, F.S., Park, Y.C., Roufa, D., and Martonosi, A. (1981). Selective stimulation of the synthesis of an 80,000-dalton protein by calcium ionophores. J Biol Chem *256*, 5309-5312.

88. Yang, J., Zong, Y., Su, J., Li, H., Zhu, H., Columbus, L., Zhou, L., and Liu, Q. (2017). Conformation transitions of the polypeptide-binding pocket support an active substrate release from Hsp70s. Nat Commun *8*, 1201.

89. Yong, J., Bischof, H., Burgstaller, S., Siirin, M., Murphy, A., Malli, R., and Kaufman, R.J. (2019). Mitochondria supply ATP to the ER through a mechanism antagonized by cytosolic Ca(2). Elife *8*.

90. Zheng, H., Cooper, D.R., Porebski, P.J., Shabalin, I.G., Handing, K.B., and Minor, W. (2017). CheckMyMetal: a macromolecular metal-binding validation tool. Acta Crystallographica Section D *73*, 223-233.
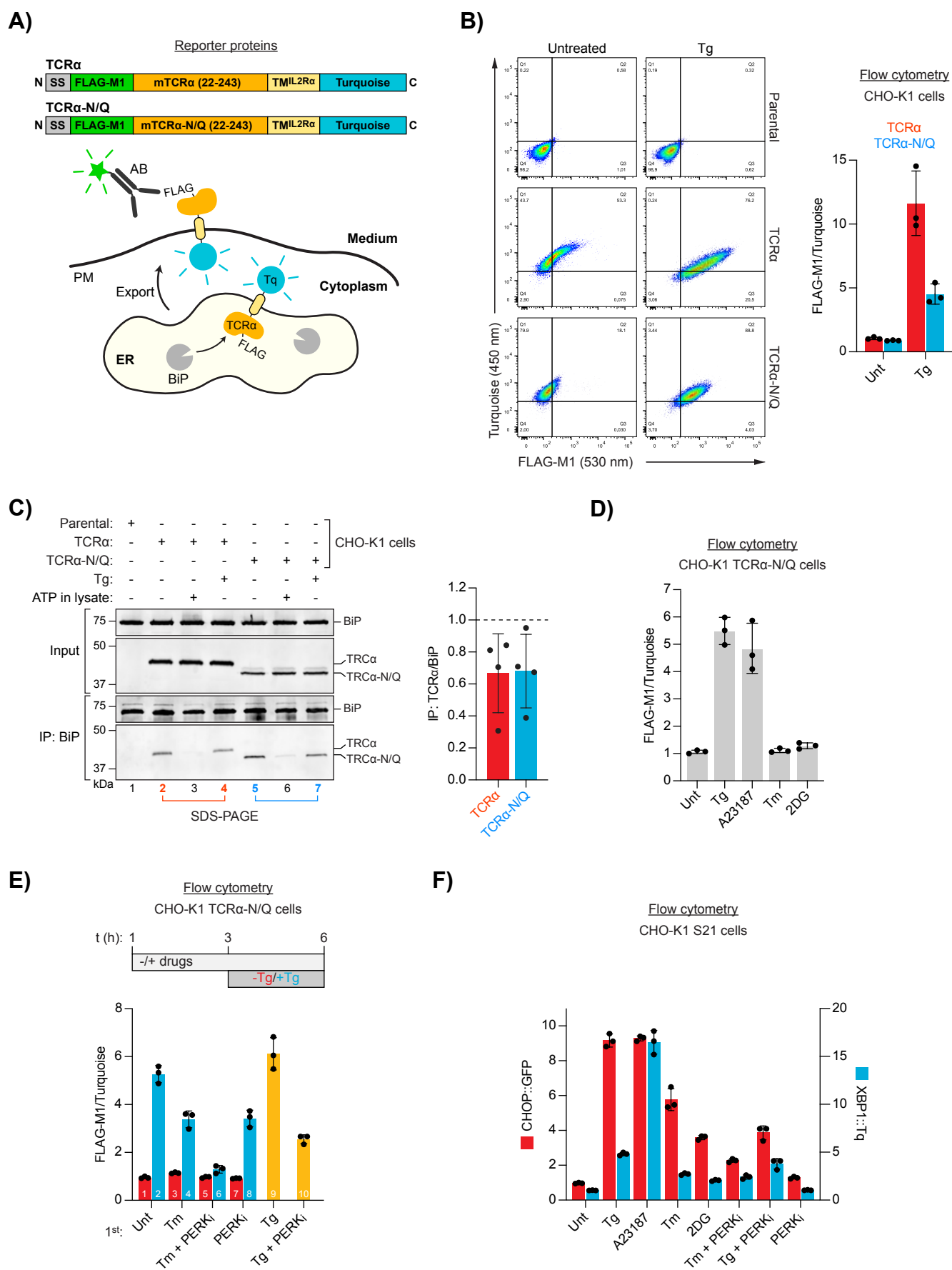
Figure 1

Figure 1

ER Ca^{2+} depletion-dependent trafficking of TCRα-based reporter proteins

A) Schematic representation of reporter proteins and detection principles. Signal sequence (SS); FLAG-M1 epitope tag; mouse T-cell antigen receptor α chain (mTCRα); transmembrane domain of the interleukin 2 receptor α subunit (TM^{IL2Rα}); monomeric Turquoise (Tq); endoplasmic reticulum (ER); plasma membrane (PM).

B) Flow cytometry analysis of TCRα cell surface exposure. CHO-K1 cell lines stably expressing TCRα or glycosylation-deficient TCRα-N/Q were left untreated or exposed to Thapsigargin (Tg) for 3 h before analysis. Dot plots of a representative experiment are shown. Graph: reporter surface exposure is plotted as the ratio between the FLAG-M1 and Turquoise median fluorescence signal (relative to a data point of TCRα in untreated cells arbitrarily set to 1). Bars represent mean ± SD from three independent experiments.

C) Co-immunoprecipitation (IP) of TCRα reporter proteins with BiP from stable CHO-K1 cell lines (as in '**B**') analysed by SDS-PAGE and immunoblotting. Where indicated cells were treated with Tg for 3 h prior to lysis. ATP was depleted from samples during lysis to stabilise BiP-substrate interactions except from the sample marked with 'ATP' to which additional ATP was added instead. Graph: ratios of the quantified blot signals relative to untreated samples (set to 1; dashed line). Bars represent mean ± SD from four independent experiments.

D-E) Flow cytometry analysis as in '**B**'. (**D**) Cells were treated for 3 h, as indicated, before analysis [tunicamycin (Tm); 2-deoxyglucose (2DG)]. (**E**) Cells were exposed to the compounds indicated. After 3 h the medium was replaced by medium containing the same compounds without (red) or with additional Tg (blue) for further 3 h before analysis. Samples 9 and 10 (yellow bars) contained the same amount of Tg before and after medium exchange. PERK inhibitor (PERK$_i$). Bars: mean ± SD from three independent experiments.

F) Flow cytometry analysis of a UPR reporter CHO-K1 cell line (S21) carrying a predominantly PERK-controlled CHOP::GFP marker and a predominantly IRE1-controlled XBP1::Turquoise marker. The cells were treated for 6 h, as indicated. Median fluorescence signals relative to untreated cells are shown. Bars: mean ± SD from three independent experiments.
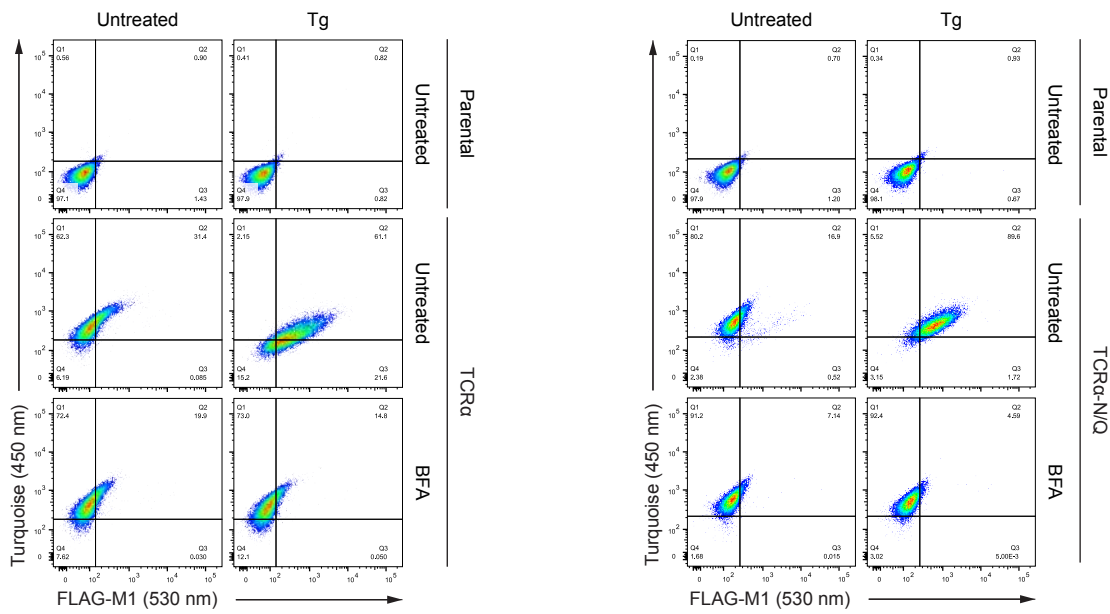
Figure 1-figure supplement 1

Figure 1-figure supplement 1

Brefeldin A blocks exposure of the TCRα reporter on the cell surface

Dot plots of a representative flow cytometry analysis of CHO-K1 cells stably expressing TCRα or TCRα-N/Q after treatment with Thapsigargin (Tg) and brefeldin A (BFA) for 3 h, as indicated.
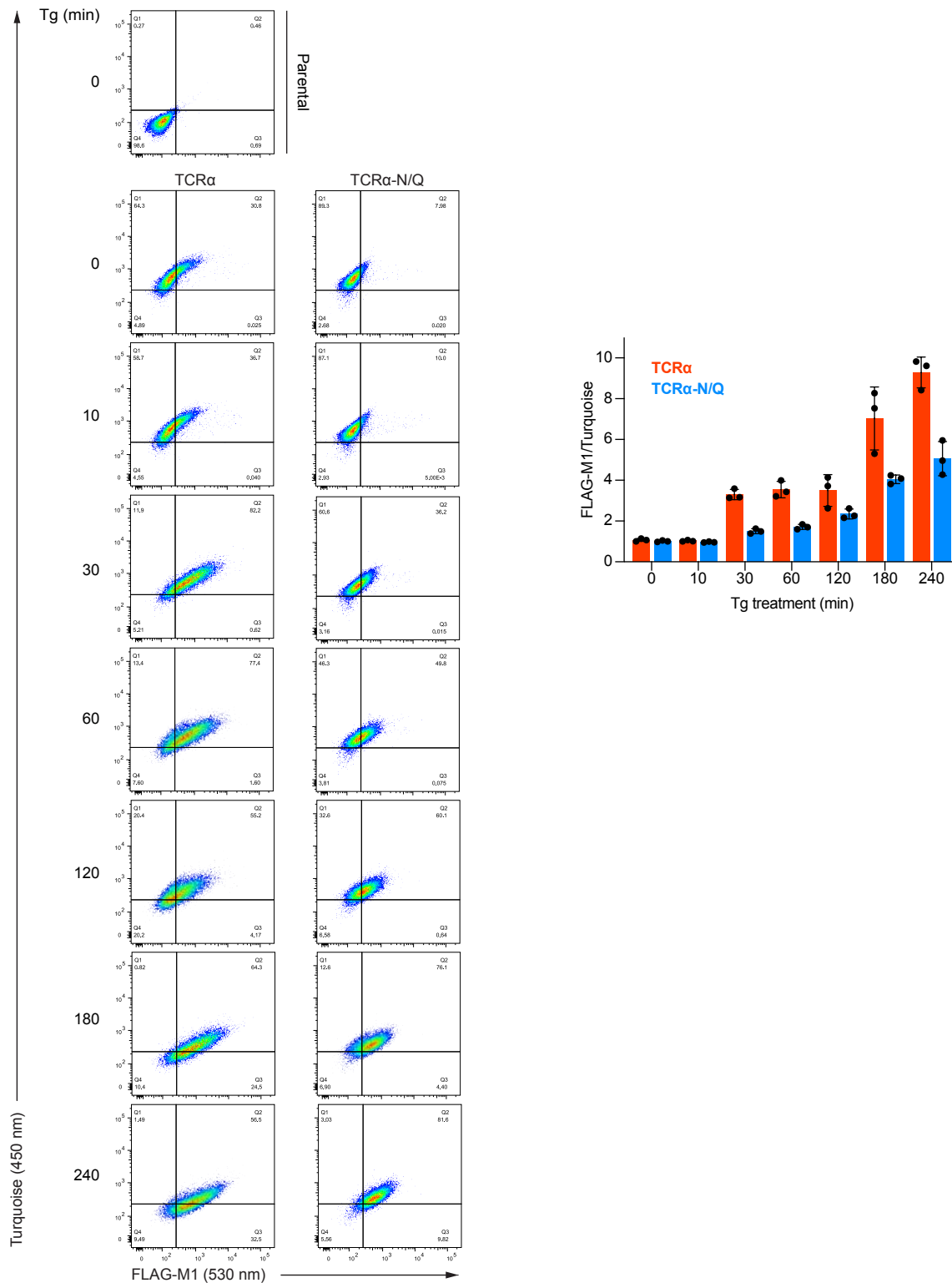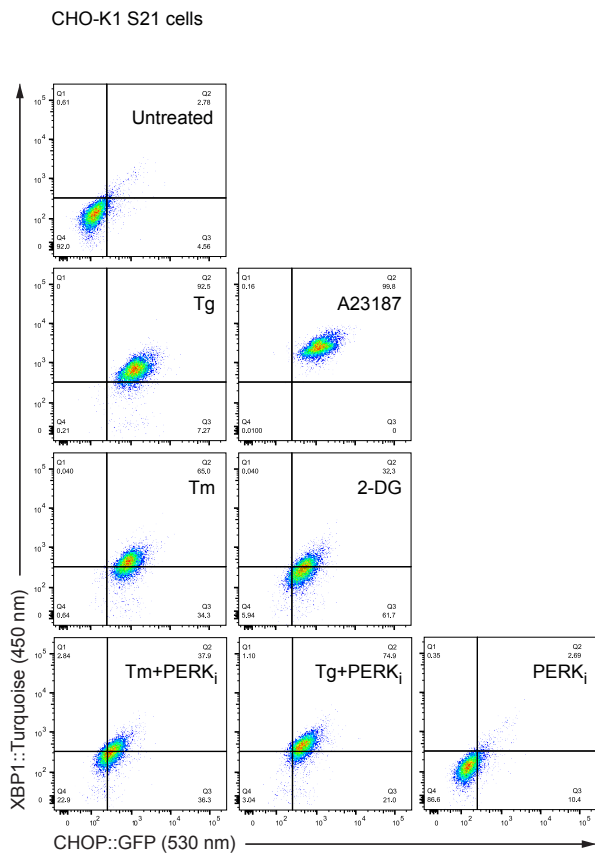
Figure 1-figure supplement 2

Figure 1-figure supplement 2

Time course of exposure of the TCRα reporter on the cell surface during ER Ca^{2+} depletion

Dot plots of a representative flow cytometry analysis of CHO-K1 cells stably expressing TCRα or TCRα-N/Q after treatment with Thapsigargin (Tg) for indicated periods. Graph: reporter surface exposure is given as the ratio between the FLAG-M1 and Turquoise median fluorescence signal relative to untreated cells. Bars: mean ± SD bars are shown from three independent experiments.

Figure 1-figure supplement 3

Figure 1-figure supplement 3

ER Ca²⁺ depletion and ER stress induce the UPR

Dot plots of a representative flow cytometry experiment using CHO-K1 CHOP::GFP XBP1::Tq cells (S21). The cells were treated for 6 h, as indicated. Related to **Figure 1F**.

Figure 2

A)

B)

C)

ATP hydrolysis: 5 µM BiP + 3 mM MgCl$_2$ + 2 mM ATP

47
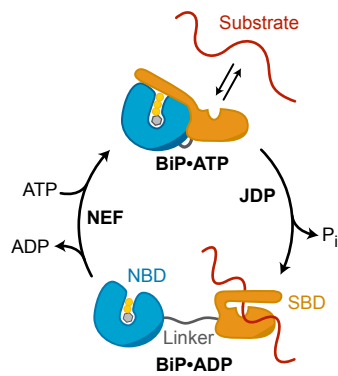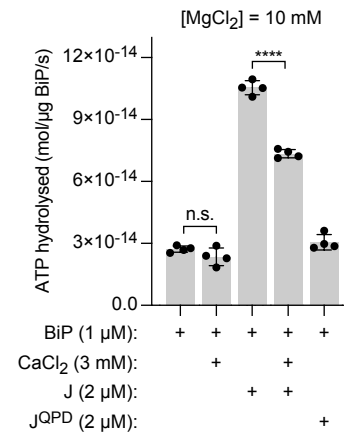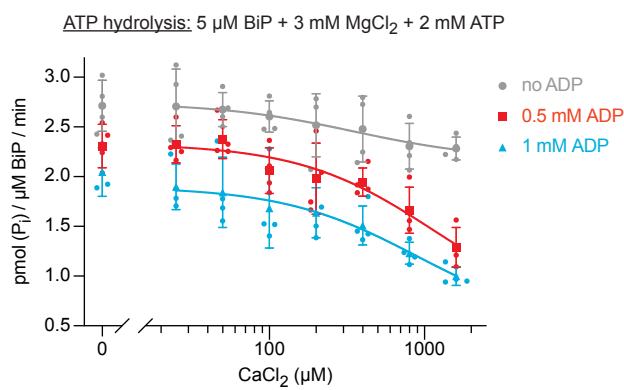
Figure 2

Effect of Ca^{2+} on BiP's ATPase activity

A) Schematic representation of BiP's chaperone cycle. Unfolded substrate protein (red); nucleotide binding domain (NBD); substrate binding domain (SBD); interdomain linker (grey); orthophosphate (P$_i$); J-domain protein (JDP); nucleotide exchange factor (NEF).

B) ATP hydrolysis by purified BiP measured with a NADH-based ATPase assay. All samples contained 10 mM MgCl$_2$ and 1 μM BiP. Where indicated CaCl$_2$ (3 mM) and wildtype (J) or mutant J-domain (J^{QPD}) were added (both at 2 μM). Bars: mean $\pm$ SD from four independent experiments. **** $p < 0.0001$, 95% CI -3.672e^{-14} to -2.695e^{-14}, two-tailed, unpaired, parametric t-test.

C) ATPase activity of BiP measured by detection of ATP hydrolysis product (P$_i$) accumulation using a malachite green-based assay. All samples contained 3 mM MgCl$_2$ and 2 mM ATP. CaCl$_2$ was titrated (0 - 1.6 mM). Where indicated samples contained 0.5 mM (red) and 1 mM (blue) ADP. Bold symbols represent mean values $\pm$ SD derived from individual data points (staggered dots). Best-fit lines are shown.
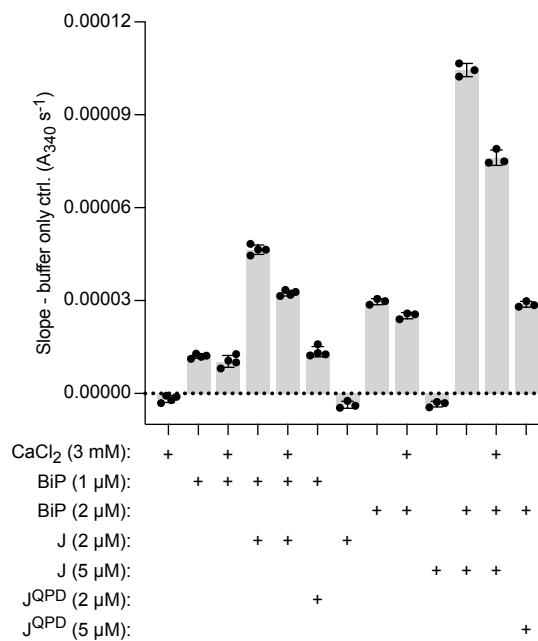
Figure 2-figure supplement 1

A)

B)

bioRxiv preprint doi: https://doi.org/10.1101/2020.11.03.366484; this version posted November 3, 2020. The copyright holder for this preprint (which was not certified by peer review) is the author/funder, who has granted bioRxiv a license to display the preprint in perpetuity. It is made available under a CC-BY-NC-ND 4.0 International license.
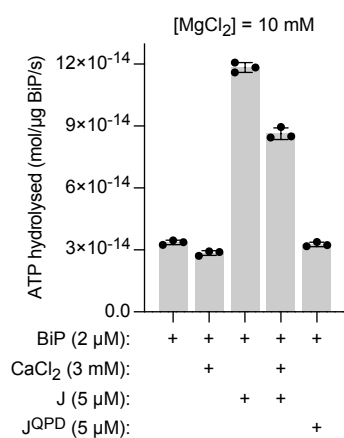
Figure 2-figure supplement 1

Effect of Ca^{2+} on BiP's ATPase activity measured by a NADH-based assay

ATP hydrolysis by purified BiP measured with a NADH-based ATPase assay that detects ADP production. All samples contained 10 mM MgCl$_2$. Where indicated CaCl$_2$ (3 mM) and wildtype or mutant J-domain (J; J^{QPD}) were added.

(**A**) Same as **Figure 2B** but with higher protein concentrations. Bars: mean $\pm$ SD from three independent experiments.

(**B**) Slopes of time-dependent NADH signals (absorbance at 340 nm; A$_{340}$) of experiments shown in '**A**' and **Figure 1B**. The value of the 'buffer only' control reaction was subtracted in each experiment. Bars: mean $\pm$ SD from at least three independent experiments. Note: the reaction velocity correlates with the BiP concentration.
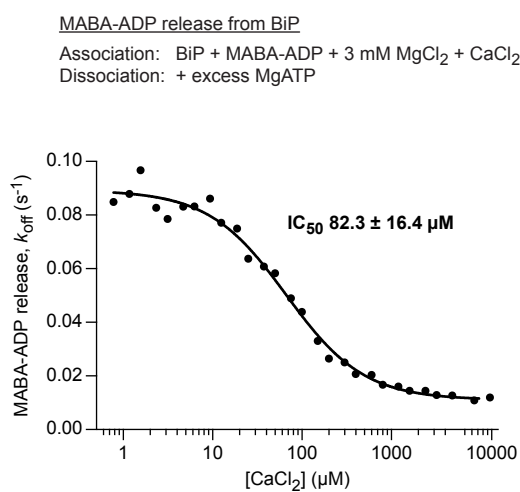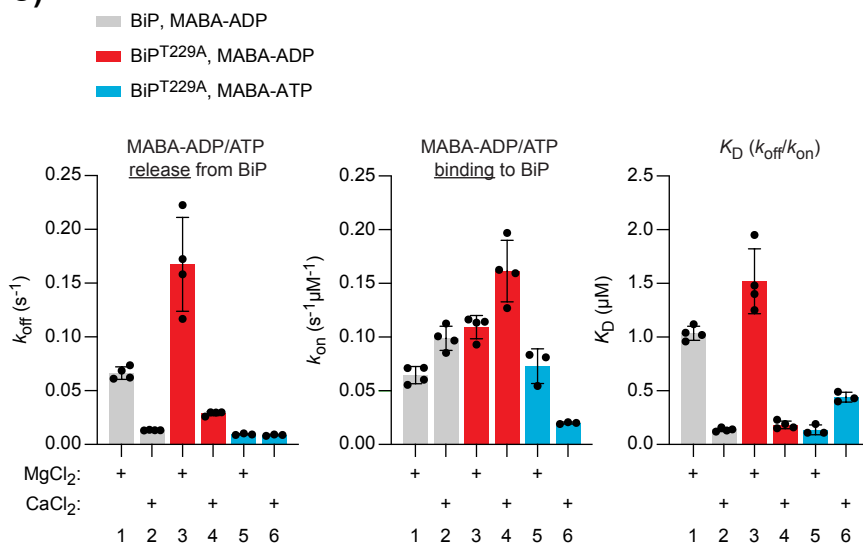
Figure 3

A)

MABA-ADP release from BiP

Solution A
(BiP + MABA-ADP + X)
↓
Incubate (≥ 1 h)
(association)
↓
Mix A with solution B
(excess MgATP) in a 11:1 ratio
at t = 0
↓
Measure MABA-ADP dissociation
(Ex/Em 360/440 nm)

t: -1 h   Association (3 mM MgCl₂)   0   Dissociation

1: BiP + MABA-ADP | + MgATP
2: BiP + MABA-ADP | + MgATP + CaCl₂
3: BiP + MABA-ADP + CaCl₂* | + MgATP
4: BiP + MABA-ADP | + MgATP + Grp170
5: BiP + MABA-ADP + CaCl₂* | + MgATP + Grp170

* [CaCl₂] 1 mM

B)

MABA-ADP release from BiP

Association: BiP + MABA-ADP + 3 mM MgCl₂ + CaCl₂
Dissociation: + excess MgATP

IC_{50} 82.3 ± 16.4 μM

C)

BiP, MABA-ADP
BiP^{T229A}, MABA-ADP
BiP^{T229A}, MABA-ATP

MABA-ADP/ATP release from BiP

MABA-ADP/ATP binding to BiP

K_D (k_{off}/k_{on})

51

Figure 3

Differential effect of Ca^{2+} on ATP and ADP binding to BiP

A) Representative plot of fluorescence against time of pre-formed complexes of MABA-ADP and BiP (each 1.3 µM) challenged at t = 0 with excess of MgATP (1.5 mM) to reveal nucleotide release. All solutions contained 3 mM $MgCl_2$. $CaCl_2$ (1 mM) and Grp170 (1.3 µM) were added at t = -1 or t = 0 as indicated. Graph: mean MABA-ADP dissociation rate constants (k_{off}) $\pm$ SD from three independent experiments (the curved line connecting conditions 1 & 4 and 3 & 5 emphasises the effect of calcium on the activity of Grp170).

B) MABA-ADP dissociation rates from BiP plotted against [$CaCl_2$] of a representative experiment. The experiment was performed as in '**A**'. All samples contained $MgCl_2$ (3 mM). $CaCl_2$ was present at increasing concentrations during nucleotide binding (solution A). The half maximal inhibitory concentration (IC_{50}) of $CaCl_2$ (mean $\pm$ SD) was calculated from three independent experiments.

C) Effect of Ca^{2+} on affinities of nucleotides for BiP. The dissociation rates of MABA-ADP and MABA-ATP from wildtype or ATPase-impaired T229A mutant BiP were measured as in '**A**', whereby either $MgCl_2$ or $CaCl_2$ (1 mM) were present throughout the experiment (solutions A and B). The association rate constants (k_{on}) were measured upon addition of MABA-labelled nucleotides to BiP in presence of either divalent cation. The dissociation constants (K_D) were calculated based on the rate constants (k_{off}/k_{on}). Nucleotide-free proteins were used. Bars: mean $\pm$ SD. All the data points from $\geq$ 3 independent experiments are shown.

Figure 3-figure supplement 1

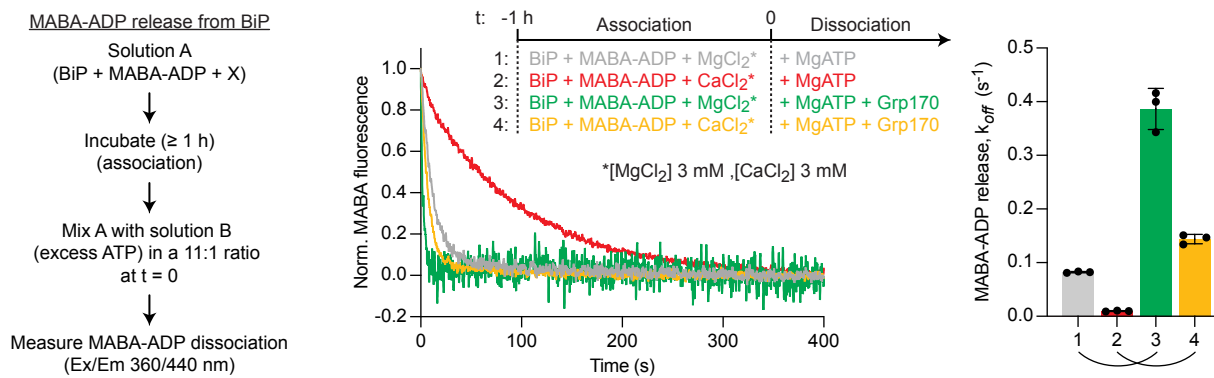## Figure 3-figure supplement 1

**Dissociation BiP•MABA-ADP complexes formed in presence of either Mg^{2+} or Ca^{2+}**

Representative plot of fluorescence against time of complexes of MABA-ADP and BiP (each 1.3 µM) formed in presence of either $MgCl_2$ or $CaCl_2$ (each 3 mM). Excess of MgATP (1.5 mM) without or with Grp170 (1.3 µM) was added at t = 0 to reveal nucleotide release. Graph: mean MABA-ADP dissociation rate constants (k_{off}) $\pm$ SD from three independent experiments. Final concentrations after mixing are given. Note: the stronger stimulatory effect of Grp170 compared to **Figure 3A** may be due to variations in the experimental conditions.

Figure 4

A)
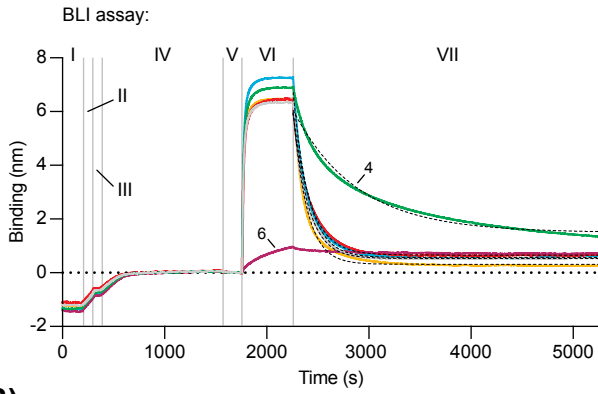
Steps:	I.	Sensor equilibration
	II.	J or J^{QPD} loading
	III.	Wash
	IV.	P15 peptide loading
	V.	Baseline
	VI.	BiP association
	VII.	BiP dissociation

	VI. Association (BiP +)	VII. Dissociation
1	$MgCl_2$ + ATP	$MgCl_2$ + ATP
2	$MgCl_2$ + $CaCl_2$ + ATP	$MgCl_2$ + ATP
3	$MgCl_2$ + ATP	$MgCl_2$ + $CaCl_2$ + ATP
4	$MgCl_2$ + ATP	$MgCl_2$ + ADP
5	$MgCl_2$ + ATP	$CaCl_2$ + ATP
6	$MgCl_2$ + ATP (J^{QPD})	$MgCl_2$ + ATP

Conc. 1.5 mM ATP, 1.5 mM ADP, 3 mM $MgCl_2$, 1 mM $CaCl_2$
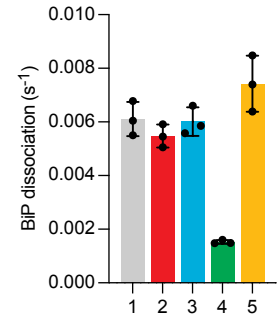
B)
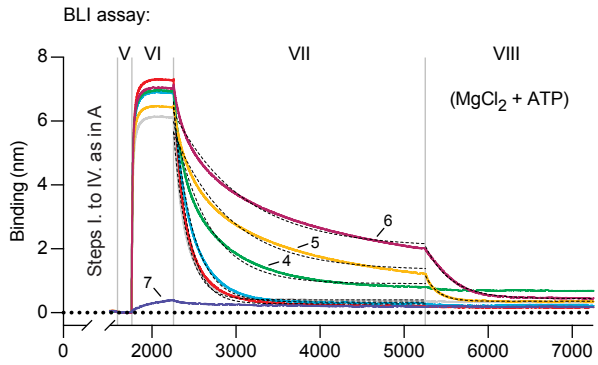
VI. Association: BiP + $MgCl_2$ + ATP

VII. Dissociation

1	$MgCl_2$ + ATP
2	$MgCl_2$ + $CaCl_2$ + ATP
3	$MgCl_2$ + ATP + ADP
4	$MgCl_2$ + $CaCl_2$ + ATP + ADP
5	$MgCl_2$ + ADP
6	$CaCl_2$ + ADP
7	$MgCl_2$ + ATP (J^{QPD})

Conc. 1.5 mM ATP, 0.75 mM ADP, 3 mM $MgCl_2$, 1 mM $CaCl_2$

55

Figure 4

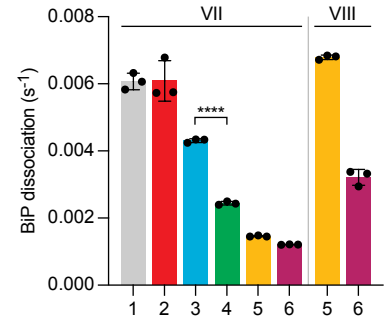## Ca^{2+} affects ATP-dependent dissociation of substrates from BiP

A-B) A representative plot of the Bio-Layer interferometry (BLI) signal against time. The individual steps of the experiment (I-VII) are indicated: following an initial equilibration step (I) biotinylated wildtype or QPD mutant J-domain protein was immobilized corresponding to an interference signal difference of ∼0.4 nm (II). After a wash step (III) the sensors were saturated with biotinylated P15 BiP substrate peptide (IV). After a stable baseline signal was established (V) the sensors were transferred into solutions containing BiP to measure association in presence of ATP (VI). Dissociation of BiP from the sensor was measured in protein-free solutions containing either ADP or ATP (VII). The composition of solutions in steps VI and VII as well as the concentrations of the variable components are indicated. (**A**) MgCl$_2$ and/or CaCl$_2$ were present where indicated. Dashed lines represent single exponential fit curves. Graph: mean dissociation rate constants (k_{off}) ± SD from three independent experiments. (**B**) Same as '**A**' but with identical solutions for all sensors in step VI and varying solution compositions in step VII. In the additional step (VIII) the sensors were introduced into solutions containing ATP and MgCl$_2$. **** $p < 0.0001$, 95% CI -0.00198822 to -0.00174311, two-tailed, unpaired, parametric t-test.
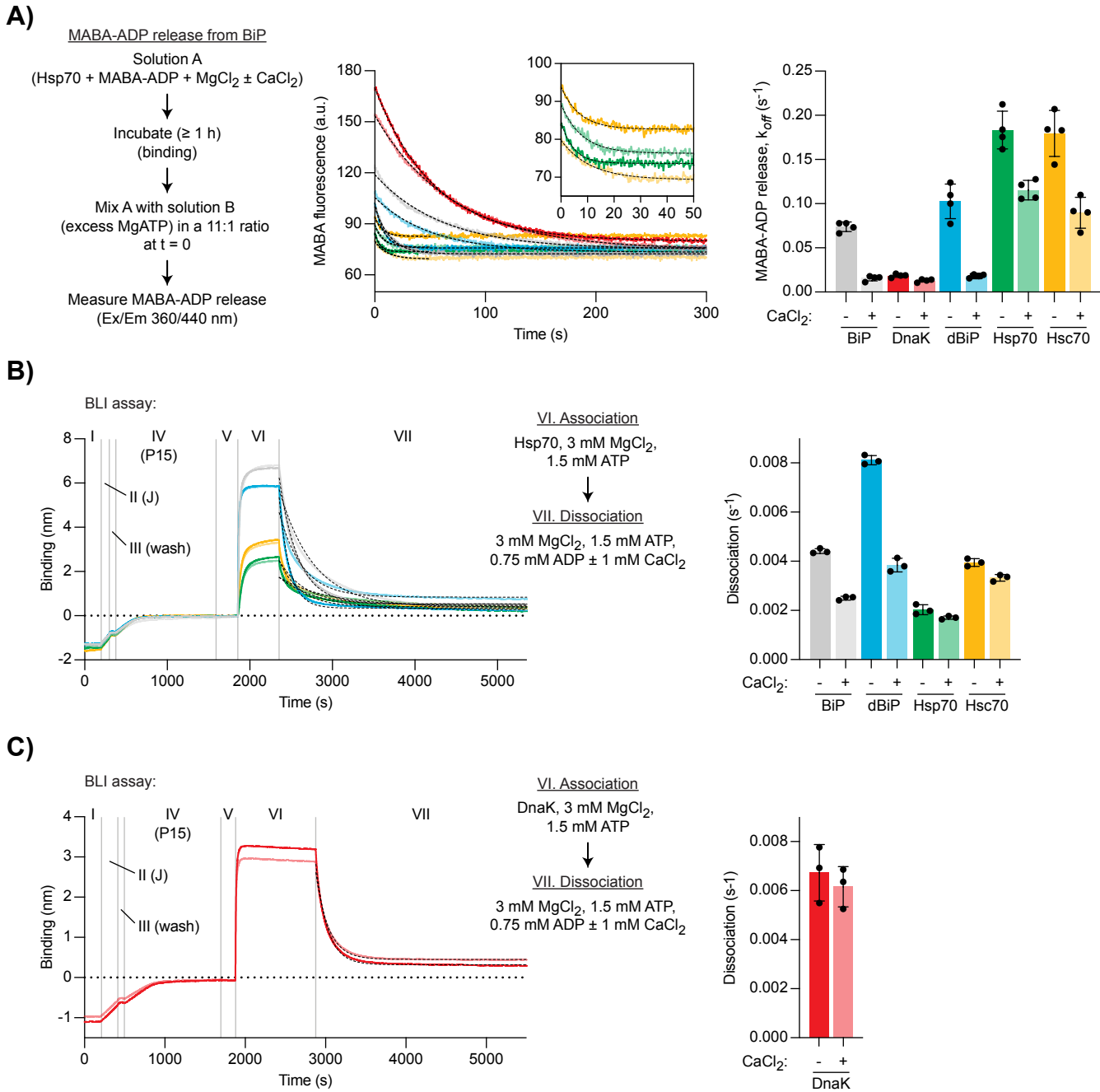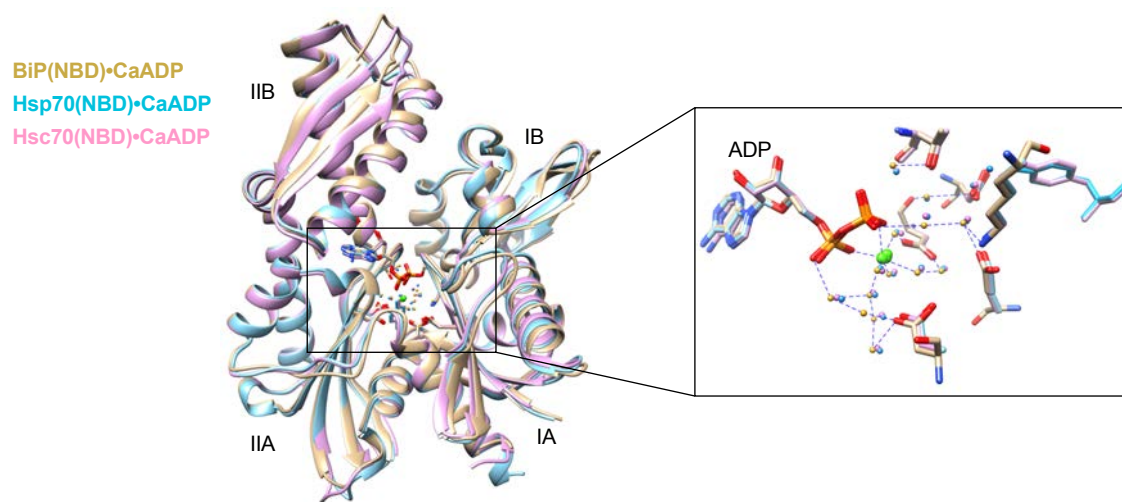
Figure 5

Figure 5

Ca²⁺ selectively stabilises BiP•ADP compared with cytoplasmic Hsp70s

A) Representative plot of fluorescence against time of complexes of MABA-ADP and indicated full-length Hsp70 chaperones (each 1.3 µM) formed without or with $CaCl_2$ (1 mM) (dBiP, *Drosophila* BiP). All solutions contained $MgCl_2$ (3 mM). Excess of MgATP (1.5 mM) was added at t = 0 to reveal MABA-ADP release. Final concentrations are given. Graph: mean MABA-ADP dissociation rate constants (k_{off}) $\pm$ SD from four independent experiments.

B-C) A representative plot of the Bio-Layer interferometry (BLI) signal against time. The experiments were performed as in **Figure 4A** with the indicated Hsp70s. Dissociation of Hsp70s from the sensor was measured in protein-free solutions (VII). The composition of solutions in steps VI and VII as well as the concentrations of the variable components are indicated. (**B**) Analysis of eukaryotic Hsp70s. Dashed lines represent single exponential fit curves. Graph: mean dissociation rate constants (k_{off}) $\pm$ SD from three independent experiments. (**C**) Same as '**B**' but with *E. coli* DnaK.

Figure 6
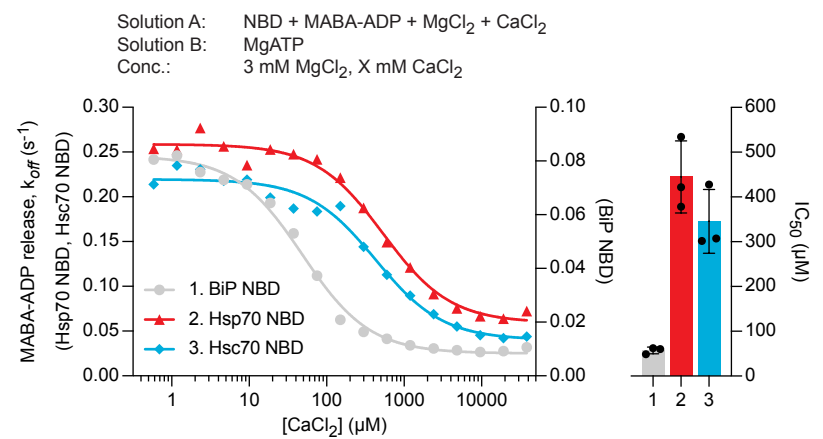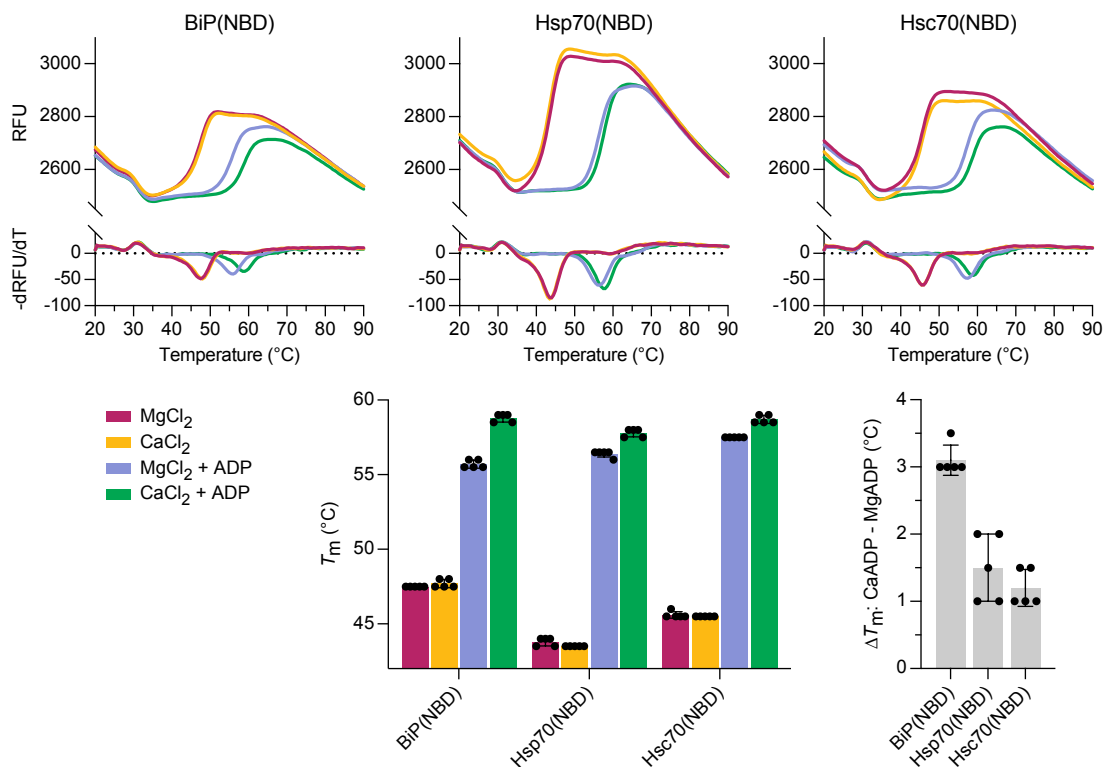
A)

B)
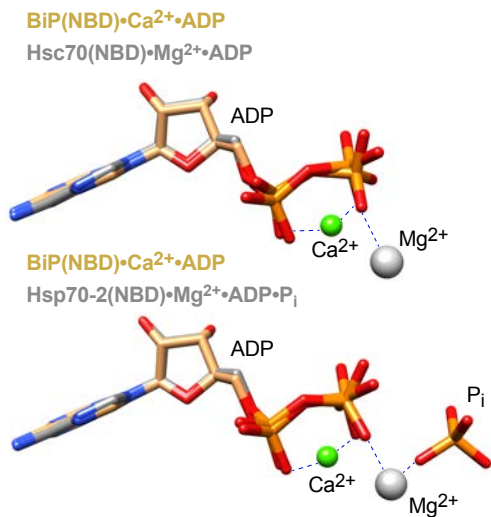
C)

D)

Figure 6

Structural analysis of Ca^{2+} and ADP binding to Hsp70 nucleotide binding domains

A) Ribbon diagram of the aligned crystal structures of BiP (yellow), Hsp70 (blue) and Hsc70 (pink) nucleotide binding domains (NBD) in complex with Ca^{2+} and ADP. The subdomains IA-IIB are indicated. Inset: coordination of Ca^{2+} ions (green) by water (small spheres) and ADP in the nucleotide binding cleft.

B) Nucleotide and metal ion ligands of BiP(NBD)•Ca^{2+}•ADP (as in '**A**') and bovine Hsc70(NBD) •Mg^{2+}•ADP (PDB 1BA1) or human Hsp70-2(NBD)•Mg^{2+}•ADP•P_i (PDB 3I33) based on nucleotide alignment. ADP, inorganic phosphate (P_i), Ca^{2+} (green sphere), and Mg^{2+} (grey sphere) are shown.

C) MABA-ADP dissociation rates from the indicated NBDs plotted against [$CaCl_2$] of a representative experiment. The experiment was performed as in **Figure 3A**. All samples contained $MgCl_2$ (3 mM). $CaCl_2$ was present at increasing concentrations during NBD•MABA-ADP complex formation. Bars: the half maximal inhibitory concentration (IC_{50}) of $CaCl_2$ (mean $\pm$ SD) was calculated from three independent experiments.

D) Melting temperatures (T_m) of the indicated NBDs (at 5 µM) were measured by differential scanning fluorimetry (DSF) in presence of $MgCl_2$ or $CaCl_2$ (each 6 mM) without or with ADP (4 mM). Top: representative melt curves with their negative first derivatives (RFU, relative fluorescence units). Left bar graph: mean T_m ± SD of three independent experiments. Right bar graph: difference in T_m (ΔT_m) between MgADP and CaADP containing samples.
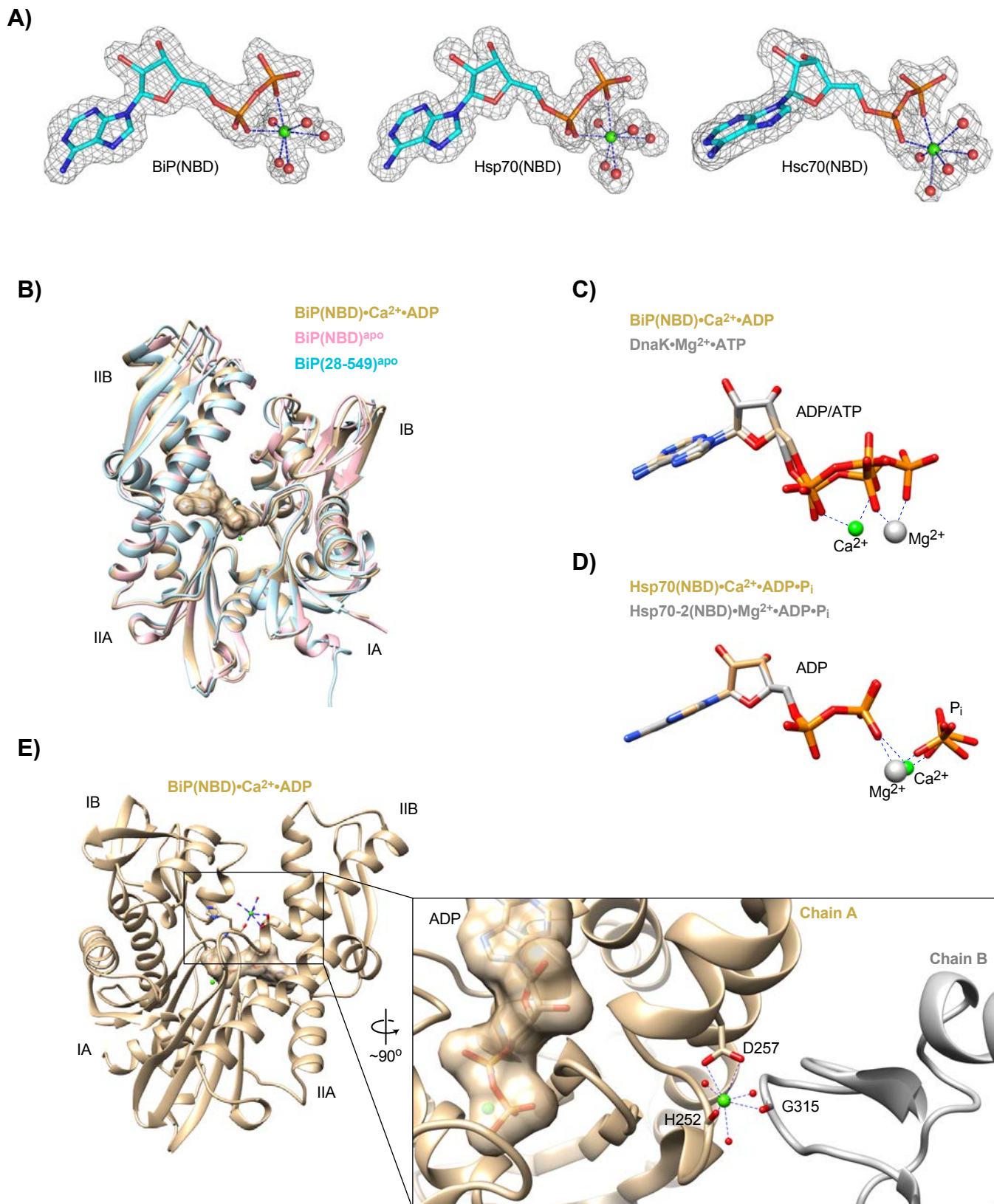
Figure 6-figure supplement 1

Figure 6-figure supplement 1

Structural details of nucleotide binding domains and their ligands

A) Polder OMIT maps (grey mesh) of BiP, Hsp70, and Hsc70 nucleotide binding domain (NBD) ligands omitting ADP (sticks), Ca^{2+} (green sphere), and water molecules (red spheres) contoured at 3.80 RMSD and including density within 1.6 Å of all atoms shown.

B) Ribbon diagram of NBDs of (i) BiP(NBD)•Ca^{2+}•ADP aligned with (ii) BiP(NBD)^{apo} (PDB 3LDN) (RMSD i vs. ii 0.75 over 336 C_α) and (iii) BiP(28-549)^{apo} (PDB 6HAB) (RMSD i vs. iii 0.776 over 311 C_α). The nucleotide is shown in surface representation and the Ca^{2+} ion (green sphere) is indicated.

C) Nucleotide and metal ion ligands of BiP(NBD)•Ca^{2+}•ADP and DnaK•Mg^{2+}•ATP (PDB 4B9Q) based on nucleotide alignment. ADP, ATP, Ca^{2+} (green sphere), and Mg^{2+} (grey sphere) are shown.

D) Nucleotide and metal ion ligands of human Hsp70-2(NBD)•Mg^{2+}ADP•P_i (PDB 3I33) and human Hsp70(NBD)•Ca^{2+}•ADP•P_i (PDB 1S3X) based on nucleotide alignment. ADP, Ca^{2+} (green sphere), and Mg^{2+} (grey sphere) are shown.

E) Ribbon diagram showing coordination of a surface-bound Ca^{2+} ion (green sphere) in the BiP(NBD) structure, involving contacts to the crystallographic neighbouring molecule (chain B; grey). Relevant water molecules (red spheres) as well as ADP (surface representation) and Ca^{2+} within the nucleotide binding cleft are indicated. A Ca^{2+} ion was also identified at the corresponding surface position in structures of Hsp70(NBD) and Hsc70(NBD). In neither case does this Ca^{2+} ion participate in coordination of the nucleotide.
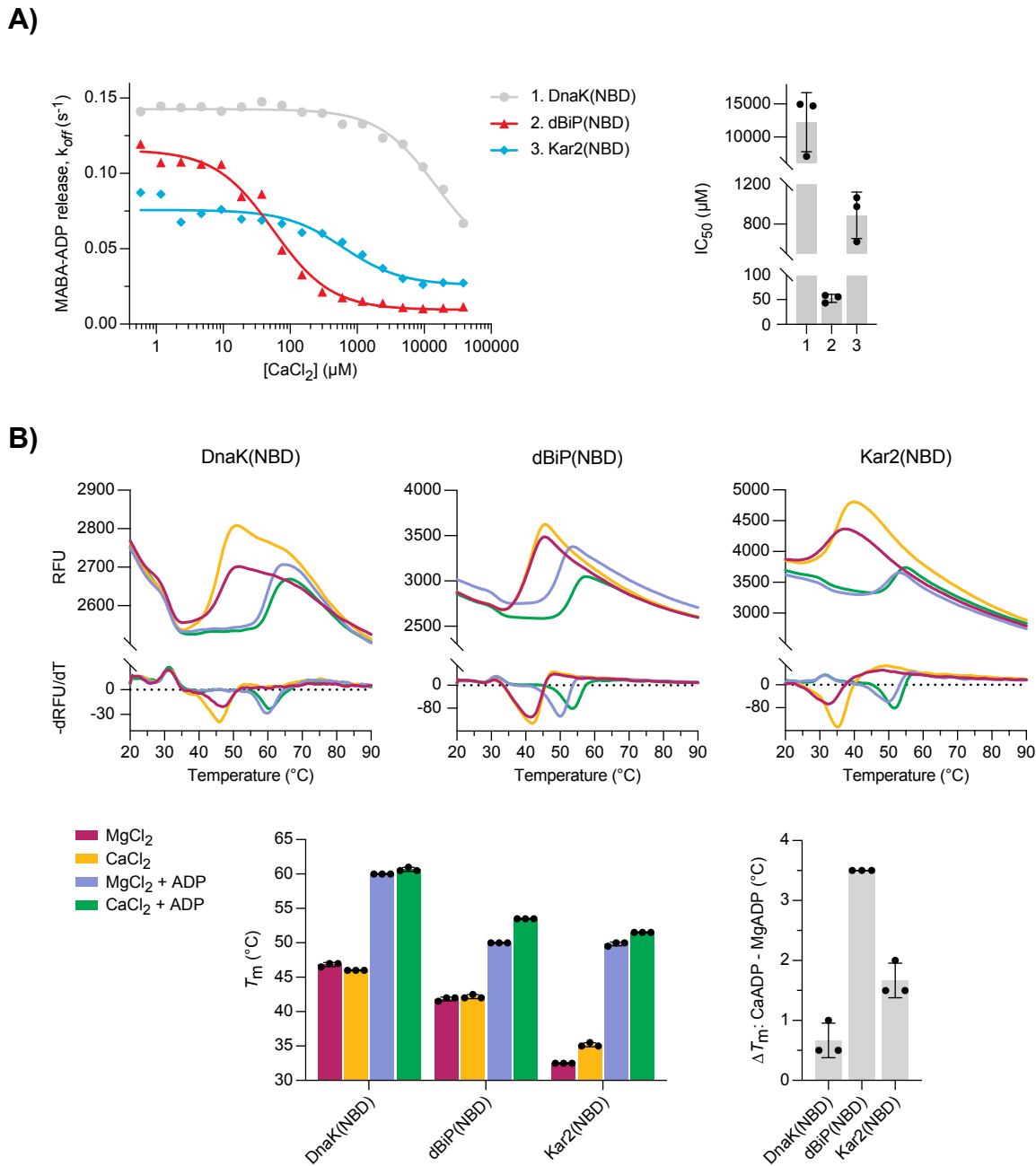
Figure 6-figure supplement 2

A)

B)

Figure 6-figure supplement 2

Characterisation of nucleotide binding domains of *Drosophila* BiP, DnaK, and Kar2

A) MABA-ADP dissociation rates from the indicated NBDs plotted against [$CaCl_2$] of a representative experiment. The experiment was performed as in **Figure 3A**. All samples contained $MgCl_2$ (3 mM). $CaCl_2$ was present at increasing concentrations during NBD:MABA-ADP complex formation. Graph: the half maximal inhibitory concentration (IC_{50}) of $CaCl_2$ (mean $\pm$ SD) was calculated from three independent experiments.

B) Melting temperatures (T_m) of the indicated NBDs (at 5 µM) were measured by differential scanning fluorimetry (DSF) in presence of $MgCl_2$ or $CaCl_2$ (each 6 mM) without or with ADP (4 mM). Top: representative melt curves with their negative first derivatives (RFU, relative fluorescence units). Left bar graph: mean $T_m \pm$ SD of three independent experiments. Right bar graph: difference in T_m (ΔT_m) between MgADP and CaADP containing samples.
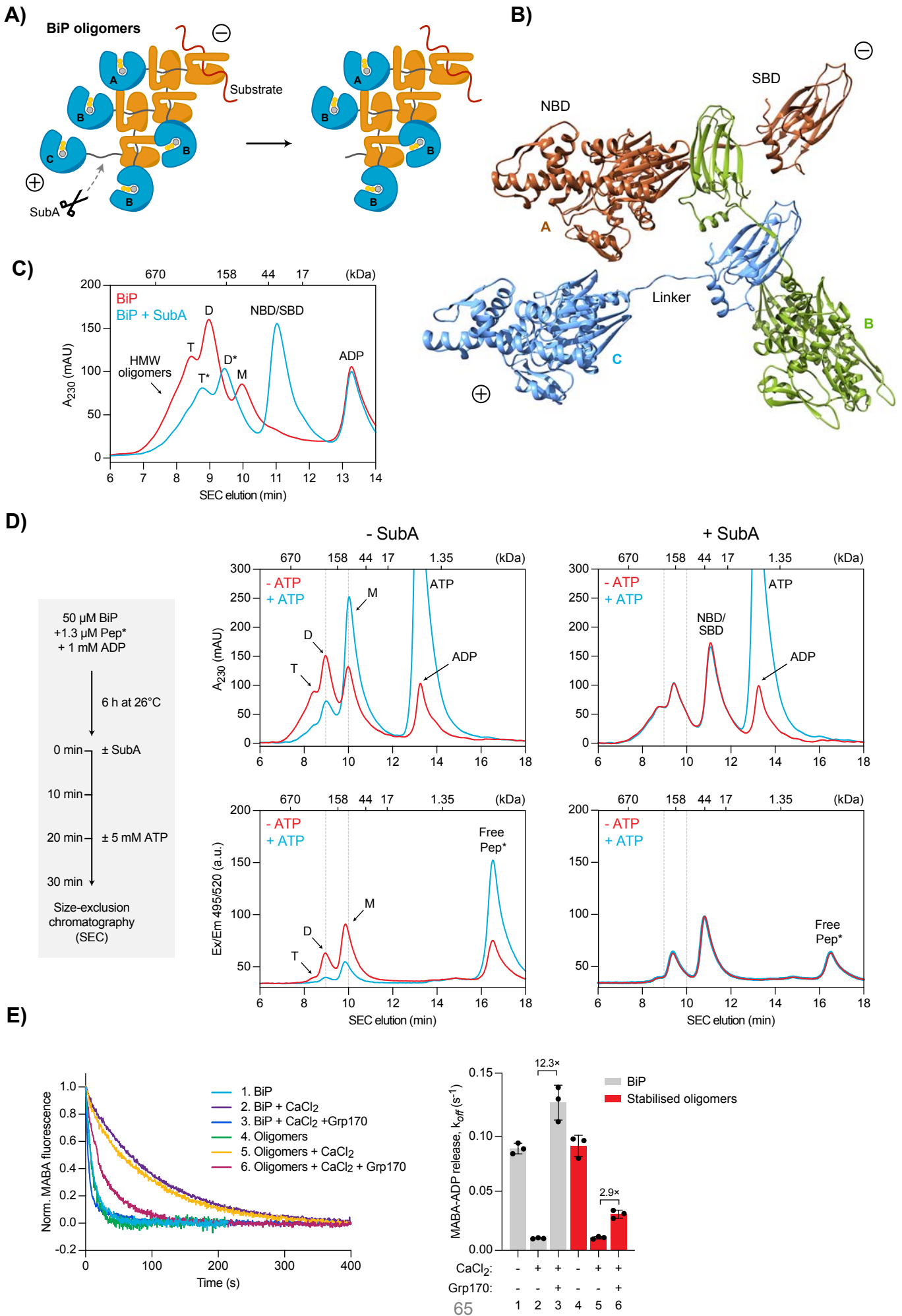
Figure 6-figure supplement 2

Figure 7

Figure 7

Effect of calcium on BiP oligomers in vitro

A) Schematic representation of BiP oligomers. Unfolded substrate protein (red) and the distinct types of BiP protomers (A, B and C) are shown. Oligomers are directional assemblies with minus (-) and plus (+) ends. The cleavage site for the BiP linker-specific protease SubA (scissors) is only accessible on (+)-end protomer (C). The predicted inert BiP oligomer lacking the C protomer nucleotide binding domain (a result of SubA cleavage) is shown on the right.

B) Ribbon diagram of apo BiP$^{T229A-V461F}$ oligomers formed by typical substrate interactions between protomers. Three protomers (labelled A-C according to '**A**') are presented in different colours.

C) Size-exclusion chromatography (SEC) elution profile of BiP. BiP was incubated with ADP (1 mM) and where indicated treated with SubA before SEC. Monomeric (M), dimeric (D), and trimeric BiP (T) is indicated. Heterogenous high molecular weight (HMW) BiP complexes elute early as a shoulder. Note that the peaks of proteolytic cleavage products originating from trimers and dimers (*) are shifted to later elution times. Also note the disappearance of BiP monomers and a new peak of the individual nucleotide and substrate binding domains (NBD and SBD) after treatment with SubA.

D) SEC elution profile as in '**C**' of BiP and substrate peptide. BiP was incubated with trace amounts of fluorescently labelled substrate peptide (NR; Pep*) in presence of ADP at indicated concentrations. Where indicated the samples were exposed at t = 0 to SubA for 30 min before SEC. Where indicated excess of ATP was added 10 min before SEC. Peptide bond absorbance at 230 nm (A$_{230}$) and the fluorescence signal of the labelled peptide were recorded separately.

E) Representative plot of fluorescence against time of complexes of MABA-ADP and BiP or purified, stabilised BiP oligomers (each 1.3 µM) formed in presence of either MgCl$_2$ or CaCl$_2$ (each 3 mM). Excess of ATP (1.5 mM) without or with Grp170 (1.3 µM) was added at t = 0 to reveal nucleotide release. Graph: mean MABA-ADP dissociation rate constants (k_{off}) ± SD from three independent experiments. Final concentrations are given.

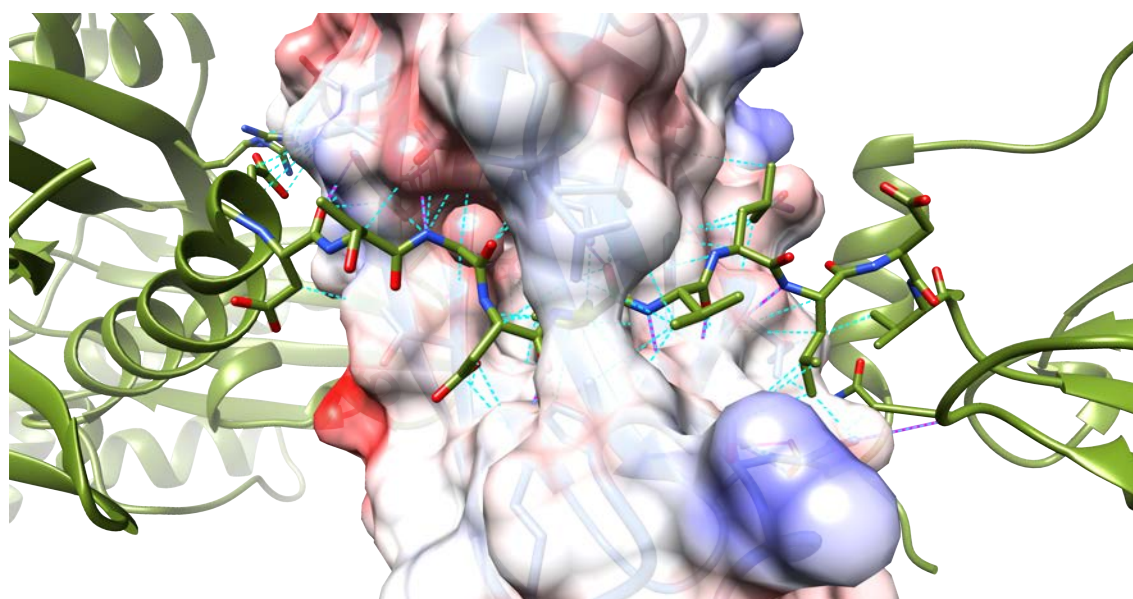# Figure 7-figure supplement 1

A)
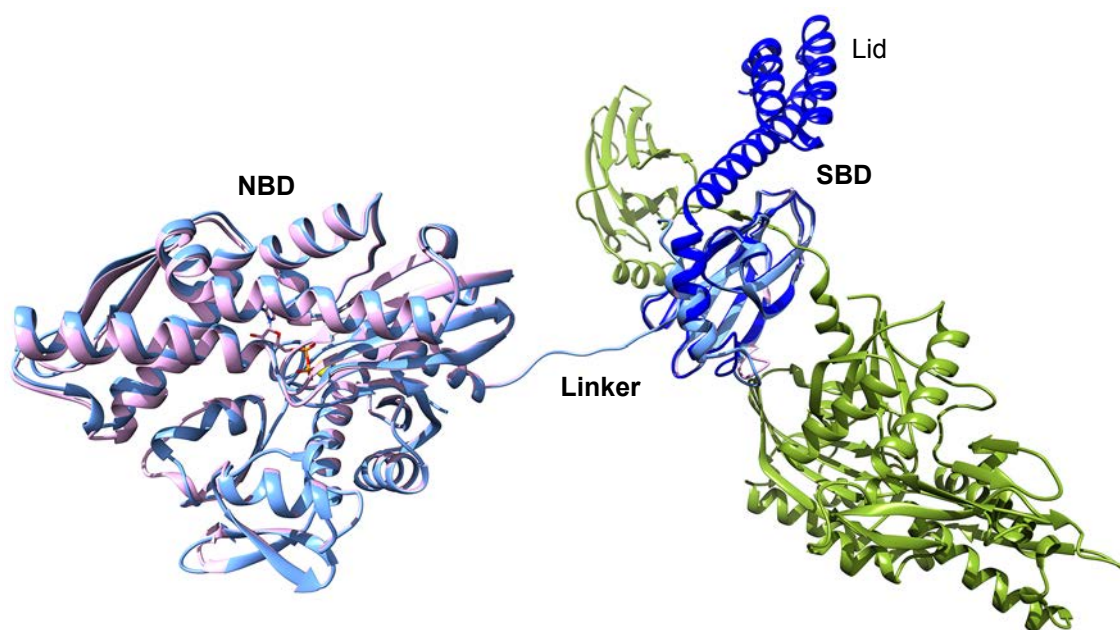
B)

Figure 7-figure supplement 1

Structural features of oligomeric BiP

A) Superposition of the asymmetric unit of a lid-truncated ADP-bound oligomeric BiP (pink) onto the biological (dimeric) assembly of oligomeric apo-BiP protomers (light blue and green, as in Figure 7B) reveals a highly similar conformation. ADP is shown in stick form with its coordinating K^+ ion (yellow sphere). The isolated substrate binding domain (SBD) of DnaK, including the C-terminal lid structure in the closed conformation (dark blue; PDB 1DKZ), is also aligned and reveals only minor conformational differences to the lid-truncated SBD of oligomeric BiP.

B) Close-up view of the interdomain linker of one BiP protomer (green) bound to the SBD of another BiP protomer as in 'A'. The surface of the linker-binding SBD is shown with translucent coulombic surface colouring. All residues participating in trans-protomer interactions are shown as sticks. Hydrogen bonds are highlighted with solid magenta pseudo bonds and van der Waals interactions are represented by cyan dashed pseudo bonds. Note that the majority of the linker side chains occupy the hydrophobic surface of the substrate binding groove and most polar bonds are to mainchain amide atoms of the β-sheet scaffold of the SBD.
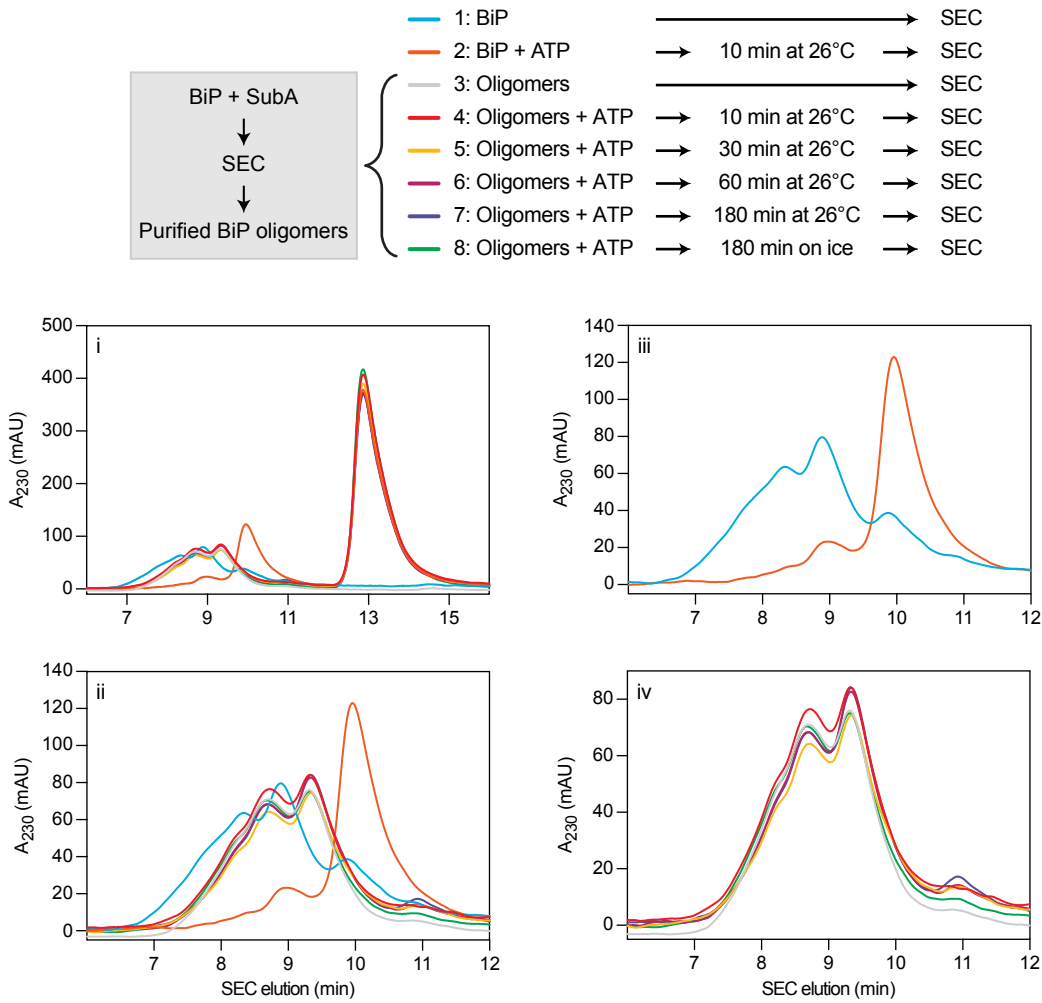
Figure 7-figure supplement 2

Preissler et al.

Figure 7-figure supplement 2

Stability of purified BiP oligomers after cleavage with SubA, assessed by size-exclusion chromatography

Size-exclusion chromatography (SEC) elution profile of BiP or purified BiP oligomers. BiP oligomers were isolated after cleavage by SubA and frozen. Thawed samples were exposed to ATP for indicated times before SEC analysis. As a control, uncleaved BiP was loaded. Note that purified BiP oligomers were stable in presence of ATP.

Panels 'ii – iv' represent different detailed views of the chromatogram shown in 'i'.
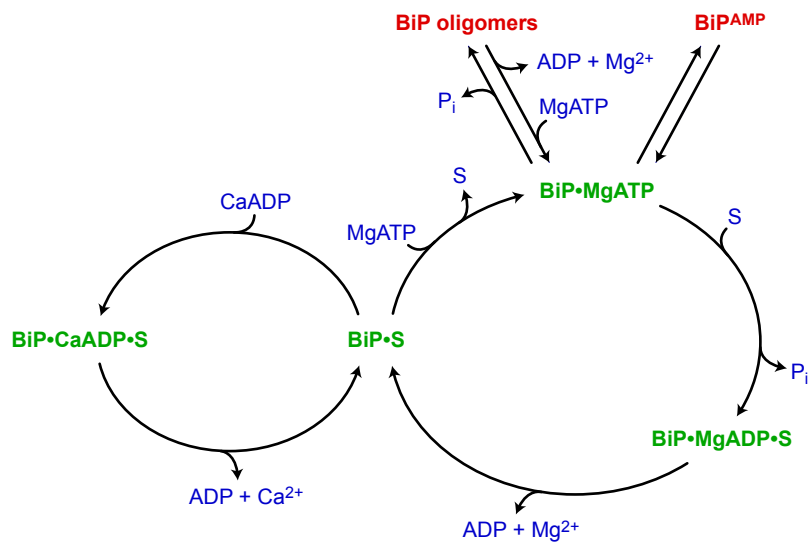
Figure 8

Figure 8

Calcium-dependent alternative fates of BiP during nucleotide exchange

The interaction of BiP with its substrates (S) is driven by an ATPase-dependent chaperone cycle, whereby ATP binding triggers substrate release and ATP hydrolysis (to ADP and orthophosphate; P_i) induces high-affinity substrate binding (right cycle). Re-binding of ADP (instead of ATP) to BiP during post-hydrolysis nucleotide exchange stabilises the interaction between BiP and substrate (left cycle). Because Ca^{2+} enhances the affinity of ADP for BiP, and ADP competes with ATP for binding to BiP, substrate interaction-stabilising ADP-to-ADP exchange cycles are favoured by high $[Ca^{2+}]$ and a low ATP:ADP ratio, whereas a decline in $[Ca^{2+}]$ favours ADP-to-ATP exchange and substrate release. BiP can also oligomerise into conformationally-locked (functionally inactive) assemblies by ATP hydrolysis-dependent substrate interactions amongst BiP proteins. The restricted ability of oligomeric BiP to respond allosterically to ATP binding (and the resistance of oligomeric BiP to NEF-stimulated ADP release; not shown) kinetically stabilises oligomers at the expense of heterodimeric BiP-substrate complexes in the Ca^{2+}-depleted ER. In the ATP-bound state, BiP is also subject to inactivation by reversible, covalent modification — AMPylation (BiP^{AMP}), however, this process is in competition both with recruitment of BiP to the chaperone cycle and with oligomerisation.

Table S1

	BiP NBD	Hsp70 NBD	Hsc70 NBD	Apo BiP Oligomer	ADP BiP Oligomer
Data collection					
Synchrotron stations (DLS)	I03	I04	I04	I24	I24
Space group	P1	$P2_12_12_1$	$P12_11$	$P12_11$	$P12_11$
a,b,c; Å	48.36, 51.86, 93.08	46.17, 63.71, 144.50	73.68, 78.04, 75.38	50.33, 51.29, 119.72	50.18, 51.25, 188.80
α, β, γ; ⁰	78.07, 86.72, 62.28	90.00, 90.00, 90.00	90.00, 101.26, 90.00	90.00, 100.17, 90.00	90.00, 99.77, 90.00
Resolution, Å*	29.14-1.88 (1.92-1.88)	29.53-1.52 (1.54-1.52)	73.73-1.85 (1.89-1.85)	59.92-1.77 (1.81-1.77)	29.27-1.94 (1.99-1.94)
Rmerge*	0.063 (0.989)	0.065 (0.703)	0.120 (1.005)	0.054 (0.844)	0.047 (0.533)
$<I/\sigma(I)>$*	18.2 (1.8)	14.0 (2.3)	8.9 (1.4)	9.9 (1.1)	13.7 (2.0)
CC1/2*	0.999 (0.669)	0.998 (0.814)	0.998 (0.633)	0.975 (0.531)	0.999 (0.717)
No. of unique reflections*	62200 (3792)	66932 (3125)	71566 (4400)	58872 (3347)	43705 (2937)
Completeness, %*	97.4 (90.4)	99.7 (95.1)	100.0 (100.0)	99.9 (99.8)	99.1 (94.5)
Redundancy*	8.9 (7.5)	6.7 (6.3)	6.7 (5.7)	3.2 (3.2)	3.3 (3.2)
Refinement					
Rwork/Rfree	0.209/0.225	0.196/0.212	0.218/0.247	0.185/0.217	0.184/0.226
No. of atoms (non H)	6137	3417	6399	4432	4327
Average B-factors	32.46	18.59	22.9	32.8	34.439
RMS Bond lengths Å	0.002	0.002	0.002	0.006	0.006
RMS Bond angles,⁰	1.163	1.163	1.172	1.341	1.338
Ramachandran favoured region, %	99.34	99.17	98.28	98.66	98.27
Ramachandran outliers, %	0	0	0	0	0

MolProbity score†	0.78 (100)	0.83 (100)	0.80 (100)	0.96 (100)	0.99 (100)
PDB code	6ZYH	6ZYI	6ZYJ	7A4U	7A4V

Table S1 Data Collection and refinement statistics.

*Values in parentheses are for highest-resolution shell.

†100th percentile is the best among structures of comparable resolutions. 0th percentile is the worst.

Table S2

ID	Plasmid name	Description	Encoded protein	Reference
UK173	haBiP_27-654_pQE10	Bacterial expression of His-tagged Chinese hamster BiP amino acids 27-654	BiP	PMID: 18923430
UK838	haBiP_27-654_T229A_pQE10	Bacterial expression of His-tagged ATPase deficient mutant Chinese hamster BiP amino acids 27-654	BiP^{T229A}	PMID: 26473973
UK1965	mP58_390-455_WT_AviTag_p	Bacterial expression of minimal murine ERdj6 J-domain WT amino acids 390-455 with C-term AviTag-His6	J	This study
UK1966	mP58_390-455_H422Q_AviTa	Bacterial expression of minimal murine ERdj6 J-domain amino acids 390-455 with C-term AviTag-His6 and a H422Q mutation	J^{QPD}	This study
UK1983	yUlp1(402-621)-StrepII_pET24	Bacterial expression vector for the production of yeast Ulp1 protease with a C-terminal StrepII tag	Ulp1-StrepII	PMID: 31531998
UK2039	haBiP_28-413_WT_pQE30_Sm	Bacterial expression of Chinese hamster BiP NBD (amino acids 28-413) without acidic N-term	BiP NBD	This study
UK2090	haBiP_28-549_T229A_V461F	Bacterial experssion of ATPase and substrate binding deficient, lid truncated BiP (N-terminal H6-Smt3 fusion)	Lidless BiP	This study
UK2093	hsHYPE_104-445_L258D_H363	Bacterial expression of inactive and monomeric human H363A mutant of His6-Smt3-HYPE_104-445	FICD	PMID: 31531998
UK2225	huORP150_33-999_pCA833	Bacterial expression of human ORP150/Grp170 (from Claes Andreasson) with N-terminal His6-Smt3	Grp170	Gift from Claes Andréasson lab
UK2243	pSUMO-DnaK	Bacterial expression of E. coli DnaK carrying N-terminal His6-Smt3 on a pET-24-derivative	DnaK	PMID: 29064368
UK2354	dBiP_29-635_pQE30_Smt3	Bacterial expression of Drosophila melanogaster BiP amino acids 29-635 with N-terminal His6-SUMO	dBiP	This study
UK2469	FLAGM1_TCRa_22-243_IL2RA	Mammalian expression of TCRalpha (source sequence PMID 3027582) FLAG-M1- and turquoise-tagged with a transmembrane domain of IL2RA	TCRalpha	This study
UK2470	EcDnaJ_1-72_AviTag_pET30a	Bacterial Expression of isolated J-domain of E. coli DnaJ (amino acids 1-72) as a fusion with AviTag-His6	DnaJ	This study
UK2510	pCA528-hsHsp70	Bacterial expression of full-length human HSPA1A (Hsp70) (natural variant E110D)	Hsp70	Gift from Matthias P. Mayer lab
UK2511	pCA528-hsHsc70	Bacterial expression of full-length human HSPA8 (Hsc70)	Hsc70	Gift from Matthias P. Mayer lab
UK2520	FLAGM1_TCRa_22-243_N/Q_	Mammalian expression of non-glycosylated version of TCRalpha-n/Q FLAG-M1- and turquoise-tagged with a transmembrane domain of IL2RA	TCRalpha-N/Q	This study
UK2531	pSUMO-DnaK-1-388	Bacterial expression of E. coli DnaK NBD amino acids 1-388 with N-terminal Smt3-His6 tag	DnaK NBD	This study
UK2532	pSUMO-Hsp70-1-390	Bacterial expression of human Hsp70 NBD amino acids 1-390 with N-terminal Smt3-His6 tag (natural variant E110D)	Hsp70 NBD	This study
UK2533	pSUMO-Hsc70_1-390	Bacterial expression of human Hsc70 NBD amino acids 1-390 with N-terminal Smt3-His6 tag	Hsc70 NBD	This study
UK2534	dBiP-NBD_pQE30-H6-Smt3	Bacterial expression of Drosophila melanogaster dBiP NBD with N-terminal Smt3-His6 tag	dBiP NBD	This study
UK2606	Kar2_42-433_pCA528_pET24a	Bacterial expression Saccharomyces cerevisiae Kar2 NBD amino acids 42-433 with N-terminal Smt3-His6 tag	Kar2 NBD	This study